

# The geography of numerical mixing in a suite of global ocean models

R. M. Holmes<sup>1,2\*</sup>, J. D. Zika<sup>2</sup>, S. M. Griffies<sup>3</sup>, A. McC. Hogg<sup>4</sup>, A. E. Kiss<sup>4</sup> and M. H. England<sup>1</sup>

<sup>1</sup>Climate Change Research Centre and ARC Centre of Excellence for Climate Extremes, University of New South Wales, Sydney, Australia

<sup>2</sup>School of Mathematics and Statistics, University of New South Wales, Sydney, Australia

<sup>3</sup>NOAA Geophysical Fluid Dynamics Laboratory & Princeton University Program in Atmospheric and Oceanic Sciences, Princeton, New Jersey, USA

<sup>4</sup>Research School of Earth Sciences and ARC Centre of Excellence for Climate Extremes, Australian National University, Canberra, Australia

## Key Points:

- A tracer budget residual method is presented for estimating the spatial structure of numerical mixing in global ocean models
- Numerical mixing of temperature can drive diathermal heat transport of similar magnitude to parametrized physical mixing
- Numerical mixing of temperature is prominent in the tropical thermocline and eddy active boundary current regions

---

\*Climate Change Research Centre, University of New South Wales, Sydney, Australia

Corresponding author: Ryan Holmes, [ryan.holmes@unsw.edu.au](mailto:ryan.holmes@unsw.edu.au)

## Abstract

Numerical mixing, defined here as the physically spurious diffusion of tracers due to the numerical discretization of advection, is known to contribute to biases in ocean circulation models. However, quantifying numerical mixing is non-trivial, with most studies utilizing specifically targeted experiments in idealized settings. Here, we present a precise, online water-mass transformation-based method for quantifying numerical mixing that can be applied to any conserved variable in global general circulation models. Furthermore, the method can be applied within individual fluid columns to provide a spatially-resolved metric. We apply the method to a suite of global ocean-sea ice model simulations with differing grid spacings and sub-grid scale parameterizations. In all configurations numerical mixing drives across-isotherm heat transport of comparable magnitude to that associated with explicitly-parameterized mixing. Numerical mixing is prominent at warm temperatures in the tropical thermocline, where it is sensitive to the vertical diffusivity and resolution. At colder temperatures, numerical mixing is sensitive to the presence of explicit neutral diffusion, suggesting that much of the numerical mixing in these regions acts as a proxy for neutral diffusion when it is explicitly absent. Comparison of equivalent (with respect to vertical resolution and explicit mixing parameters)  $1/4^\circ$  and  $1/10^\circ$  horizontal resolution configurations shows only a modest enhancement in numerical mixing at  $1/4^\circ$ . Our results provide a detailed view of numerical mixing in ocean models and pave the way for future improvements in numerical methods.

### Plain Language Summary:

Numerical ocean circulation models are useful tools for studying the ocean's role in climate and providing projections of climate change. However, due to constraints on computational power, numerical models must represent processes that are continuous in the real ocean using discrete approximations. One consequence of such discrete approximations is numerical mixing, whereby seawater translation (a process that should conserve properties such as heat and salt content) results in mixing and exchange of properties with surrounding seawater. Mixing in the ocean interior is weak, and so the presence of additional numerical mixing in ocean models can cause the models to drift away from reality, reducing their accuracy and utility. In this study, we present a new method for quantifying numerical mixing in global ocean models, including its three-dimensional spatial structure. Most previous quantifications of numerical mixing have been performed in idealized model configurations or have provided only bulk ocean basin-integrated estimates. We apply our method to temperature within a suite of global ocean circulation models with differing grid resolutions and model parameters. Our results will help modelers understand the consequences and trade-offs involved in choosing model parameters in order to maximize model accuracy and utility.

## 1 Introduction

Numerical ocean general circulation models are useful tools for studying ocean dynamics, interpreting observations and providing predictions of past and future circulation states (Fox-Kemper et al., 2019; S. Griffies et al., 2009). However, numerical models are necessarily approximate in that they must represent continuous physical processes using discrete operators. These discrete representations can impact the accuracy of model integrations. For example, numerical issues have been invoked to explain eastern boundary upwelling region biases in climate models (Richter, 2015), inaccurate representation of deep water circulation (Lee, Coward, & Nurser, 2002), problems with sea ice formation (Naughten et al., 2017), and the spurious uptake of heat (Adcroft et al., 2019).

## 1.1 The numerical mixing problem

In this article we focus on tracer mixing associated with the numerical representation of advection. This mixing leads to the spurious diffusion or anti-diffusion of tracer gradients, which contrasts to the continuum whereby advection, in the absence of physical mixing sources, preserves all tracer moments. Depending on their leading order truncation error, numerical advection schemes can be classed as either diffusive (e.g. first-order upwind) or dispersive (e.g. second-order centered). Dispersive advection schemes can create tracer extrema and oscillations that are particularly problematic through coupling with physical processes such as convection (S. Griffies, Pacanowski, & Hallberg, 2000; Hecht, 2010; Naughten et al., 2017). To avoid extrema creation, these schemes are usually combined with flux limiters (and/or explicit diffusion) that maintain monotonicity in the tracer distribution. However, the associated numerical diffusion can often exceed the diffusion expected in the physical system particularly in the ocean interior where physical sources of diapycnal diffusion are weak such that water-mass properties are retained over long time periods (e.g. Ledwell, Laurent, Giron, & Toole, 2011). While numerical advection schemes are increasing in sophistication, spurious numerical diffusion is still a first-order issue thought to cause problems for processes such as ocean heat uptake, transport and model drift (Adcroft et al., 2019; S. M. Griffies et al., 2015; Hill et al., 2012; Holmes, Zika, & England, 2019a; Holmes, Zika, Ferrari, et al., 2019; Ilicak, Adcroft, Griffies, & Hallberg, 2012; Lee et al., 2002; Megann, 2017).

As global ocean models move toward eddy-permitting and eddy-resolving resolutions, the importance of numerical closure schemes increases. Poorly resolved yet energetic flows near the grid-scale generally lead to enhanced spurious mixing (S. Griffies et al., 2000; Ilicak et al., 2012). Yet further increases in resolution may not necessarily be expected to reduce spurious mixing due to the down-scale cascade of enstrophy and tracer variance in geostrophic turbulence (Roberts & Marshall, 1998; Soufflet et al., 2016). Recent studies have highlighted the particular importance of lateral viscosity and momentum closure for controlling spurious mixing by arresting this cascade at scales somewhat above the grid-scale (Ilicak, 2016; Ilicak et al., 2012). However, such concerns have yet to be fully incorporated into global models where parameter choices are often made for *ad hoc* or numerical stability-based reasons.

## 1.2 Measuring numerical mixing

Much of the uncertainty around parameters and numerical schemes in ocean models may stem from the difficulty in accurately quantifying numerical mixing. In the case of relatively simple, low-order advection schemes without flux limiters, the spurious mixing due to numerical truncation can be calculated analytically (e.g. Maqueda & Holloway, 2006; Marchesiello, Debreu, & Couvelard, 2009; Soufflet et al., 2016). For non-linear and/or high-order schemes with limiters, analytical results are generally not available. In these cases, numerical experiments are needed to compare advection schemes or quantify advection processes (e.g. Burchard & Rennau, 2008; Getzlaff, Nurser, & Oschlies, 2010; Hill et al., 2012; Klingbeil, Mohammadi-Aragh, Gräwe, & Burchard, 2014).

Indirect methods of evaluating spurious mixing are often based on ideas from water-mass transformation (Groeskamp et al., 2019) where numerical mixing is inferred from changes in the distribution of volume or mass in tracer or density coordinates. However, many of these methods yield either a single global measure (e.g. Gibson, Hogg, Kiss, Shakespeare, & Adcroft, 2017; Ilicak et al., 2012) or basin-scale averages of numerical mixing whose relation to local processes is unclear (e.g. S. Griffies et al., 2000; Lee et al., 2002; Megann, 2017; Urakawa & Hasumi, 2014). These methods do not resolve the spatial structure of numerical mixing and therefore render a detailed examination of its causes rather difficult. Furthermore, many of these methods rely on estimating changes in tracer-coordinate distributions in idealized configurations where any other process that may influence that

distribution, such as surface forcing and parameterizations of subgrid-scale physical processes, are not present (e.g. S. Griffies et al., 2000; Ilicak, 2016; Ilicak et al., 2012; Riemschneider & Legg, 2007). Alternatively, the relative role of numerical and physical mixing must be estimated using parameter dependence and/or scaling arguments (e.g. Lee et al., 2002; Megann, 2017; Roberts & Marshall, 1998).

### 1.3 New approach taken here

In this article, we introduce a new method to quantify the temporal and three-dimensional spatial structure of numerical tracer mixing in realistic, global ocean models. Our method, here applied to temperature, is based on ideas from water-mass transformation. We construct a budget for what has been called the ‘internal heat content’ (Holmes, Zika, & England, 2019a, hereafter HZE19) of temperature layers within each vertical grid column. The transport of heat across isotherms due to numerical mixing can be calculated as the residual of this budget. The internal heat content provides an integrated form of the heat content which removes much of the rapid variability in the heat content of temperature layers due to adiabatic and diabatic volume exchanges. Its use for measuring spurious mixing reduces the sensitivity of our results to noise in contrast to previous approaches based on volume transports (e.g. Lee et al., 2002; Megann, 2017; Urakawa & Hasumi, 2014). Our calculations are also performed online to avoid errors associated with temporal averaging.

The diagnostic method used here could be applied to any conserved tracer field (e.g. temperature, salinity or passive tracers such as CFCs). We chose to focus on temperature given its direct connection to climate. Although our method is unable to separate the diapycnal and isopycnal components of numerical diffusion, it provides a robust and detailed picture of the impact of numerical diffusion on the model heat budget. The numerical and physical picture arising from this analysis offers the first compelling view of the geography of numerical mixing in realistic global simulations.

### 1.4 Content of this paper

The new diagnostic method is described in Section 2 and applied to a suite of MOM5-based global ocean sea-ice models described in Section 3. In contrast to studies performed in idealized contexts, which are often focused on the sensitivity to different numerical tracer and momentum advection schemes, here we make use of standard MOM5 numerical schemes employed as part of realistic global simulations. MOM5 is used widely in both ocean-only and coupled modeling projects. However, our method could equally be applied to other ocean model codes.

As we show in this study, numerical mixing drives across-isotherm heat fluxes of comparable magnitude to those associated with explicitly-parameterized mixing in all model configurations examined here. Numerical mixing is prominent in eddying regions such as the Western Boundary Currents (WBCs) and the Antarctic Circumpolar Current (ACC) as well as the tropical thermocline (Section 4). In regions of active mesoscale eddies, numerical mixing is sensitive to the presence of explicit mesoscale mixing parameterizations, particularly neutral diffusion (Section 5.1). Numerical mixing in the tropics at warm temperatures is instead sensitive to the background vertical diffusivity and the vertical grid spacing (Sections 5.2 and 5.3). Numerical mixing is most prominent at eddy-permitting resolution ( $1/4^\circ$ ), reduced at finer resolution ( $1/10^\circ$ ) and most reduced at coarse ( $1^\circ$ ) resolution (Section 5.4). However, much of this variation in numerical mixing with resolution is due to differences in explicit mixing parameters. Our results are summarized and some perspectives given in Section 6.

## 2 Methods

Our method for quantifying numerical mixing follows from the global diathermal heat budget analysis of HZE19. Here we apply the same procedure to the heat and volume budgets of the fluid within each water column that is warmer than some temperature  $\Theta^*$  (Fig. 1, where  $\Theta^*$  is an independent variable). For convenience, we work throughout the article with budgets divided by the horizontal area of the water column (an area which remains constant in time). The heat budget terms are therefore given in units of  $\text{W m}^{-2}$  and the volume budget terms are given in units of  $\text{m}^3 \text{s}^{-1} \text{m}^{-2} = \text{m s}^{-1}$ .

### 2.1 The volume budget of fluid columns

The volume per unit horizontal area of fluid (units of  $m$ ) within a fluid column warmer than  $\Theta^*$  is given by

$$\mathcal{V}(x, y, \Theta^*, t) = \int_{\Theta(x, y, z, t) > \Theta^*} dz, \quad (1)$$

where  $\Theta(x, y, z, t)$  is the temperature of the fluid column located at  $x, y$ . As defined,  $\mathcal{V}(x, y, \Theta^*, t)$  is equivalent to the depth of the  $\Theta^*$  isotherm if the column is stably stratified in temperature. However, as per traditional water mass analysis formulations (e.g. Groeskamp et al., 2019), we do not require that the fluid column be stably stratified in temperature.  $\mathcal{V}$  obeys the budget equation (see blue arrows in Fig. 1)

$$\frac{\partial \mathcal{V}}{\partial t}(x, y, \Theta^*, t) = \mathcal{G} + \mathcal{J} + \Psi, \quad (2)$$

where  $\mathcal{J}$  is the surface volume flux (per unit horizontal area) into the fluid column where the surface temperature is greater than  $\Theta^*$ ;  $\Psi$  measures the transport of volume into the column from adjacent fluid columns above the  $\Theta^*$  isotherm; and  $\mathcal{G}$  measures the volume transport, or water-mass transformation, across the  $\Theta^*$  isotherm associated with the various diabatic processes (including numerical mixing), where the associated flux convergences are once again divided by the horizontal area of the water column.

### 2.2 The heat budget of fluid columns

The heat content (per unit horizontal area in units of  $\text{J m}^{-2}$ ) of the fluid warmer than  $\Theta^*$  within each column is

$$\mathcal{H}(x, y, \Theta^*, t) = \rho_0 C_p \int_{\Theta(x, y, z, t) > \Theta^*} \Theta(x, y, z, t) dz, \quad (3)$$

where in our simulations  $\rho_0$  is a constant reference density corresponding to the Boussinesq approximation and  $C_p$  is a constant specific heat capacity (our simulations use Conservative Temperature as the prognostic temperature variable, McDougall, 2003; McDougall & Barker, 2011).  $\mathcal{H}$  obeys the budget equation (see Fig. 1)

$$\frac{\partial \mathcal{H}}{\partial t}(x, y, \Theta^*, t) = \mathcal{M} + \mathcal{N} + \mathcal{F} + \mathcal{P} + \mathcal{Q} + \rho_0 C_p \Theta^* \mathcal{G} + \mathcal{I}, \quad (4)$$

where  $\mathcal{M}$  is the diffusive heat transport across the  $\Theta^*$  isotherm due to vertical mixing,  $\mathcal{N}$  accounts for explicitly parameterized neutral diffusion,  $\mathcal{I}$  accounts for numerical mixing,  $\mathcal{F}$  accounts for surface heat fluxes where the component associated with surface volume fluxes,  $\mathcal{P}$ , is treated separately and  $\mathcal{Q}$  captures the lateral heat transport into the column from adjacent fluid columns above the  $\Theta^*$  isotherm (not including the portion associated with neutral diffusion in  $\mathcal{N}$ ). As for the volume budget, each term in Eq. (4) corresponds to a flux convergence of the given process within the volume  $\mathcal{V}$  divided by the horizontal area of the fluid column.

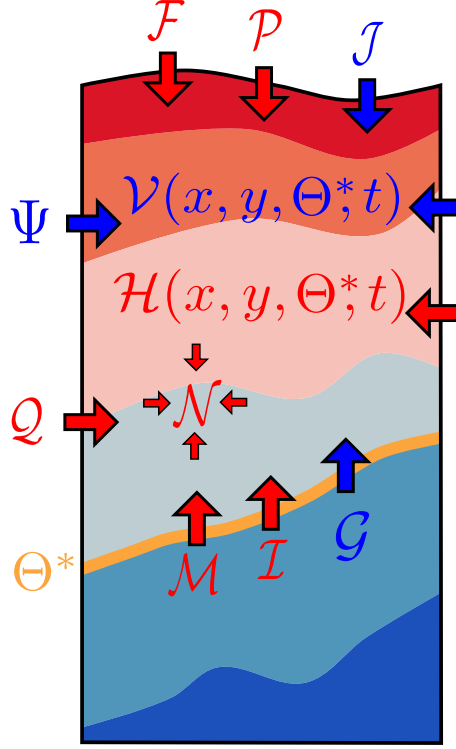


**Figure 1.** A fluid column for which budgets are constructed for the volume,  $\mathcal{V}(x, y, \Theta^*, t)$ , and heat content,  $\mathcal{H}(x, y, \Theta^*, t)$ , per unit horizontal area of water warmer than a given temperature  $\Theta^*$  (orange isotherm) [Eqs. (2) and (4)]. Each term in the budget corresponds to the convergence of the associated fluxes into the region of interest divided by the horizontal area of the fluid column, meaning that heat and volume budget terms have the units of  $\text{W m}^{-2}$  and  $\text{m s}^{-1}$  respectively. Note that we do not require the temperature stratification to be stable, although the column is drawn as such. The volume budget includes terms (blue arrows) associated with surface volume fluxes  $\mathcal{J}$ , lateral volume transport  $\Psi$  and volume transport  $\mathcal{G}$  across the  $\Theta^*$  isotherm. The heat budget includes terms (red arrows) associated with lateral heat transport  $Q$ , surface heat fluxes  $\mathcal{F}$  (where the surface heat flux associated with the surface volume fluxes  $\mathcal{P}$  is treated separately), explicitly parameterized neutral diffusion  $\mathcal{N}$ , vertical mixing  $\mathcal{M}$  and numerical mixing  $\mathcal{I}$ . Note that  $\mathcal{F}$  includes only the solar radiation that is absorbed above the  $\Theta^*$  isotherm.

### 2.3 The internal heat budget of fluid columns

It is difficult to use the full heat budget, Eq. (4), to estimate numerical mixing because of the across-isotherm volume transport term  $\mathcal{G}$ . Across-isotherm volume fluxes occur because of a convergence of the non-advective heat fluxes within temperature intervals leading to heating or cooling of the fluid within the given interval (Walsh (1982), see Eq. (14) of HZE19). The full heat budget therefore effectively includes effects of each non-advective heat flux twice; once through its diffusive flux [e.g.  $\mathcal{M}$  in Eq. (4)] and once through the across-isotherm heat transport associated with its induced across-isotherm volume transport [e.g. the contribution of  $\mathcal{M}$  to  $\mathcal{G}$  in Eq. (4)]. The second contribution through the across-isotherm volume flux can be noisy because it depends on the *convergence* (in temperature space) of the non-advective fluxes (e.g.  $\partial\mathcal{M}/\partial\Theta^*$ ). Furthermore, the contribution of across-isotherm volume fluxes to the heat budget is arbitrary in an absolute sense because it depends on the reference temperature or temperature units [being multiplied by  $\Theta^*$  in Eq. (4)].

Following HZE19, we formulate a budget for the *internal* heat content, with this budget independent of  $\mathcal{G}$ . The internal heat is defined as

$$\mathcal{H}_I(x, y, \Theta^*, t) \equiv \mathcal{H} - \rho_0 C_p \Theta^* \mathcal{V} = \rho_0 C_p \int_{\Theta^*}^{\infty} \mathcal{V} d\Theta. \quad (5)$$

Substitution of  $\mathcal{G}$  from the volume budget Eq. (2) into Eq. (4) leads to a budget for internal heat

$$\frac{\partial \mathcal{H}_I}{\partial t}(x, y, \Theta^*, t) = \mathcal{M} + \mathcal{N} + \mathcal{F} + \mathcal{P}_I + \mathcal{Q}_I + \mathcal{I}, \quad (6)$$

where

$$\mathcal{P}_I = \mathcal{P} - \rho_0 C_p \Theta^* \mathcal{J}, \quad (7)$$

$$\mathcal{Q}_I = \mathcal{Q} - \rho_0 C_p \Theta^* \Psi, \quad (8)$$

are “internal” equivalents of the surface and lateral heat transport terms, respectively.

As a consequence of the integration in Eq. (5) the internal heat content and its budget Eq. (6) are smoother and less affected by noise than the full heat content  $\mathcal{H}$  (see HZE19, in particular their Fig. A1). The internal heat content budget effectively corresponds to the integral of the volume budget multiplied by  $\rho_0 C_p$ , and it does not contain the problematic water-mass transformation volume transport  $\mathcal{G}$ . Every term in Eq. (6) can be calculated at every horizontal grid cell for any given isotherm temperature  $\Theta^*$  except the heat transport across the  $\Theta^*$  isotherm due to numerical mixing,  $\mathcal{I}(x, y, \Theta^*, t)$ . Hence, we infer  $\mathcal{I}$  by computing the residual of the other terms in the internal heat budget. The calculation provides an estimate of the transport of heat across isotherms associated with numerical mixing as a function of temperature, and time, within each fluid column. More details of how the calculation is implemented numerically are given in Appendix A, as well as a discussion of the known issues and their implications.

The area-integral of  $\mathcal{I}(x, y, \Theta^*, t)$  is the global diathermal heat transport due to numerical mixing discussed by HZE19,

$$\mathcal{I}^g(\Theta^*, t) \equiv \iint \mathcal{I}(x, y, \Theta^*, t) dx dy = \frac{\partial \mathcal{H}_I^g}{\partial t} - \mathcal{F}^g - \mathcal{P}_I^g - \mathcal{N}^g - \mathcal{M}^g, \quad (9)$$

where the relevant area element  $dx dy$  is horizontal. In the second equality we have written  $\mathcal{I}^g$  as a residual of Eq. (6), where the superscript  $g$  indicates the global area-integral under which  $\mathcal{Q}_I$  drops out.  $\mathcal{I}^g$  will be compared across our model suite in Section 5.

### 2.4 Relation to heat variance dissipation rate

Negative values of  $\mathcal{I}$ , as would be expected from a monotonic diffusive advection scheme, correspond to a down-gradient heat flux and therefore to the dissipation of tem-



perature or heat variance. This connection can be made precise by introducing a small-scale diffusive heat flux associated with the numerical mixing  $\mathbf{B}(\mathbf{x}, t)$  such that

$$\mathcal{I}^g(\Theta^*, t) = \iint_{\Theta=\Theta^*} \mathbf{B} \cdot \hat{\mathbf{n}} d\mathcal{S} = \iint_{\Theta=\Theta^*} \mathbf{B} \cdot \nabla \Theta \frac{d\mathcal{S}}{|\nabla \Theta|}. \quad (10)$$

where  $\hat{\mathbf{n}} = \nabla \Theta / |\nabla \Theta|$  and  $d\mathcal{S}$  are the normal vector and area-element of the  $\Theta^*$  isotherm respectively. Using the fundamental theorem of calculus as detailed in Marshall, Jamous, and Nilsson (1999) and Groeskamp et al. (2019), the area-integral in Eq. (10) can be converted to a volume integral,

$$\mathcal{I}^g(\Theta^*, t) = -\frac{\partial}{\partial \Theta^*} \iiint_{\Theta > \Theta^*} \mathbf{B} \cdot \nabla \Theta dV. \quad (11)$$

If  $\mathbf{B}$  is expressed in terms of a rank 2 numerical diffusivity tensor  $\mathbf{K}_{\text{num}}(\mathbf{x}, t)$  as

$$\mathbf{B}(\mathbf{x}, t) = -\rho_0 C_p \mathbf{K}_{\text{num}} \cdot \nabla \Theta, \quad (12)$$

then Eq. (11) becomes

$$\mathcal{I}^g(\Theta^*, t) = \frac{\partial}{\partial \Theta^*} \iiint_{\Theta > \Theta^*} \frac{1}{2} D^{\text{num}} dV. \quad (13)$$

The integrand of Eq. (13) is half the rate of dissipation of heat “variance”,  $\rho_0 C_p \Theta^2$ , achieved by numerical mixing as derived by Burchard and Rennau (2008),

$$D^{\text{num}} \equiv 2 \rho_0 C_p (\mathbf{K}_{\text{num}} \cdot \nabla \Theta) \cdot \nabla \Theta. \quad (14)$$

Only the symmetric component of  $\mathbf{K}_{\text{num}}$  will influence the heat variance (e.g., see chapter 13 of S. M. Griffies, 2004). There is also no guarantee that heat variance will be dissipated. A non-monotonic advection scheme can create heat variance by driving an up-gradient heat flux. Burchard and Rennau (2008) estimate  $D^{\text{num}}$  directly in three-dimensional Eulerian space by comparing the advected square of a tracer to the square of the advected tracer. Our metric  $\mathcal{I}^g$  (and its spatially resolved field  $\mathcal{I}$ ) instead corresponds to a volume integral of the heat variance dissipation rate over all fluid within a given temperature band [Eq. (13)].

## 2.5 Relation to effective diffusivity

$\mathcal{I}^g$  can also be related to the concept of an effective diffusivity used by S. Griffies et al. (2000) to quantify spurious mixing in an idealized setting. The effective diffusivity acting on temperature is defined by the vertical diffusivity  $\kappa_{\text{eff}}$  that would yield the same diathermal heat transport  $\mathcal{I}^g$  if the ocean’s temperature field was re-sorted such that isotherms were flat. That is

$$\kappa_{\text{eff}}(\tilde{z}) = - \left( \rho_0 C_p A(\tilde{z}) \frac{\partial \tilde{\Theta}}{\partial \tilde{z}} \right)^{-1} \mathcal{I}^g(\tilde{\Theta}(\tilde{z})), \quad (15)$$

where  $\tilde{\Theta}(\tilde{z})$  is the re-sorted temperature at the depth  $\tilde{z}$  and  $A(\tilde{z})$  is the area of the ocean at depth  $\tilde{z}$ .  $\kappa_{\text{eff}}$  is proportional to  $\mathcal{I}^g$  through a factor dependent on the ocean’s area and temperature distribution ( $\tilde{\Theta}(\tilde{z})$  can be easily related to  $\mathcal{V}(\Theta^*)$  and  $A(\tilde{z})$ ). However, not only is re-sorting of the temperature field problematic in a realistic global ocean model with disconnected basins, but the  $\kappa_{\text{eff}}$  so derived is a large-scale average that is not easily related to the small-scale point-wise diffusivity associated with numerical mixing that is often restricted to only small regions. The background potential energy metric of Gibson et al. (2017); Ilicak et al. (2012), or the local method of Ilicak (2016), suffer from similar issues when applied outside of an idealized setting. For these reasons, we believe that  $\mathcal{I}^g$  is a more fundamental, objective metric appropriate for a realistic global model.



## 2.6 A global metric

Integrating  $\mathcal{I}^g$  across all temperatures yields a useful summary metric for the total amount of numerical mixing within a given simulation,

$$\mathcal{I}_{\text{net}}(t) \equiv - \int_{-\infty}^{\infty} \mathcal{I}^g(\Theta^*, t) d\Theta^*. \quad (16)$$

From Eq. (11),  $\mathcal{I}_{\text{net}}$  also corresponds to the global volume integrated heat variance dissipation rate,

$$\mathcal{I}_{\text{net}}(t) = - \iiint \mathbf{B} \cdot \nabla \Theta dV. \quad (17)$$

Therefore, when globally-integrated our technique based on a temperature binning approach and the Eulerian approach of Burchard and Rennau (2008) should yield equivalent results.

## 3 Models

We analyze a suite of ocean sea-ice model simulations performed using the ACCESS-OM2 modeling framework, which couples together the Modular Ocean Model version 5.1 (MOM5) and the Los Alamos sea ice model (CICE) version 5.1.2 (Kiss et al., 2020). ACCESS-OM2 configurations are available at  $1^\circ$  (ACCESS-OM2-1),  $1/4^\circ$  (ACCESS-OM2-025) and  $1/10^\circ$  (ACCESS-OM2-01) horizontal resolution. Forcing is taken from the JRA55-do reanalysis (Tsujino et al., 2018) and consists of a repeating cycle of the period May 1990 - April 1991 (Stewart et al., 2019). We use 13 different model configurations (see Table 1) to test sensitivity to horizontal and vertical resolution, the vertical diffusivity, neutral physics parameterizations and lateral viscosity. More information on ACCESS-OM2 is contained in Kiss et al. (2020). Below we note details particularly relevant to the current study.

In all models vertical diffusion of both tracers and momentum is parameterized using a background diffusivity, the K-profile parameterization (Large, McWilliams, & Doney, 1994) and a bottom-enhanced internal tide mixing scheme (Simmons, Jayne, Laurent, & Weaver, 2004). All configurations utilize the multi-dimensional piece-wise parabolic tracer method (MDPPM, Colella & Woodward, 1984) for horizontal tracer advection, with a monotonicity-preserving flux limiter following Suresh and Huynh (1997). Horizontal momentum advection uses a centered 2nd-order method, and horizontal friction is implemented with a biharmonic operator and a Smagorinsky scaling for the viscosity coefficient (S. M. Griffies & Hallberg, 2000).

To evaluate sensitivity to the neutral physics parameterizations we compare three configurations of ACCESS-OM2-025 where the GM eddy transport parameterization is active or inactive (with a spatial structure determined according to the “baroclinic zone” setting, see S. M. Griffies, 2012; S. M. Griffies et al., 2005), or neutral diffusion in the form of a neutral diffusivity (Redi, 1982; Solomon, 1971) is active or inactive. When active, the ACCESS-OM2-025 simulations use a maximum (minimum) GM diffusivity of  $200 \text{ m}^2 \text{ s}^{-1}$  ( $1 \text{ m}^2 \text{ s}^{-1}$ ) and a neutral diffusivity that is scaled by the grid spacing relative to the local Rossby radius with a maximum value of  $200 \text{ m}^2 \text{ s}^{-1}$ . All ACCESS-OM2-1 configurations utilize a maximum (minimum) GM diffusivity of  $600 \text{ m}^2 \text{ s}^{-1}$  ( $50 \text{ m}^2 \text{ s}^{-1}$ ) and a spatially constant neutral diffusivity of  $600 \text{ m}^2 \text{ s}^{-1}$ .

Sensitivity to the background vertical diffusivity is examined by comparing ACCESS-OM2-025 simulations with no background diffusivity, with a constant value of  $10^{-5} \text{ m}^2 \text{ s}^{-1}$  and with a latitudinally dependent structure following Jochum (2009) with  $5 \times 10^{-6} \text{ m}^2 \text{ s}^{-1}$  in the mid- and high-latitudes reducing to  $10^{-6} \text{ m}^2 \text{ s}^{-1}$  near the Equator. The background vertical viscosity is  $10^{-4} \text{ m}^2 \text{ s}^{-1}$  in all simulations.

**Table 1.** A summary of the various model configurations. KDS refers to vertical level positions chosen according to Stewart et al. (2017) while GFDL50 indicates the GFDL CM2.5 vertical levels scheme.  $\kappa_v$  indicates the background vertical diffusivity, with J09 indicating a reduction to  $10^{-6} \text{ m}^2 \text{ s}^{-1}$  within the equatorial band (Jochum, 2009). GM refers to the eddy-transport scheme of Gent and McWilliams (1990) and ND refers to explicit neutral diffusion. Each configuration is initialized from the World Ocean Atlas 2013 version 2 (WOA13) and spun-up for the time period shown in the second last column (except for ACCESS-OM2-01-hvise which was initialized from ACCESS-OM2-01 and run for only two years). The last column lists the globally-integrated heat variance dissipation rate due to numerical mixing metric  $\mathcal{I}_{\text{net}}$  discussed in Section 2.6.

Configuration	Horizontal spacing	Vertical levels	Background $\kappa_v$ ( $\text{m}^2 \text{s}^{-1}$ )	Neutral physics	Spin-up (analysis) years	$\mathcal{I}_{\text{net}}$ ( $\text{PW}^\circ\text{C}$ )
025	$1/4^\circ$	KDS50	0	none	162 (10)	19.6
025-N	$1/4^\circ$	KDS50	0	ND	162 (10)	15.8
025-NG	$1/4^\circ$	KDS50	0	ND+GM	162 (10)	14.9
025-NG-kb5	$1/4^\circ$	KDS50	$10^{-5}$	ND+GM	164 (10)	10.8
025-NG-kbv	$1/4^\circ$	KDS50	$5 \times 10^{-6}$ (J09)	ND+GM	164 (10)	13.0
025-KDS75	$1/4^\circ$	KDS75	$10^{-6}$	none	162 (10)	16.3
1-KDS50	$1^\circ$	KDS50	$5 \times 10^{-6}$ (J09)	ND+GM	320 (10)	7.8
1-GFDL50	$1^\circ$	GFDL50	$5 \times 10^{-6}$ (J09)	ND+GM	320 (10)	7.5
1-KDS75	$1^\circ$	KDS75	$5 \times 10^{-6}$ (J09)	ND+GM	320 (10)	6.3
1-KDS100	$1^\circ$	KDS100	$5 \times 10^{-6}$ (J09)	ND+GM	320 (10)	5.5
1-KDS135	$1^\circ$	KDS135	$5 \times 10^{-6}$ (J09)	ND+GM	320 (10)	4.9
01	$1/10^\circ$	KDS75	$10^{-6}$	none	162 (2)	14.7
01-hvise	$1/10^\circ$	KDS75	$10^{-6}$	none	2 (1)	13.1

Sensitivity to the vertical resolution is evaluated by comparing five ACCESS-OM2-1 configurations with 50 to 135 vertical levels using two different level position schemes.

Finally, we also compare the standard ACCESS-OM2-01 configuration to a configuration where the non-dimensional Smagorinsky scaling coefficient for the lateral viscosity is increased from  $C = 2$  to  $C = 3$  (ACCESS-OM2-01-hvise).

#### 4 Spatial structure of numerical mixing in ACCESS-OM2-025

We start by examining properties of numerical mixing in the ACCESS-OM2-025 configuration. This configuration has the most numerical mixing across the model suite ( $\mathcal{I}_{\text{net}} = 19.6 \text{ PW } ^\circ\text{C}$ , Table 1). Numerical mixing makes the dominant contribution to the globally-integrated diathermal heat transport contributing for example 0.86 PW, which is 68% of the peak transport of 1.28 PW, at  $21.5^\circ\text{C}$  (compare black and blue lines in Fig. 2). Numerical mixing is significant at all temperatures. The main features of the internal heat content budget shown in Fig. 2 are consistent with the MOM025 Control simulation discussed by HZE19. ACCESS-OM2-025 has similar parameter settings to the zero background diffusivity simulation discussed by HZE19, which are also consistent with the parameter settings used in the ocean component of the GFDL CM2.5 climate model (with an exception being the vertical grid; see Section 5.3).

In this section we discuss the spatial structure of the numerical mixing in ACCESS-OM2-025 using the diagnostic method discussed in Section 2. In Fig. 3a-c we show estimates of the heat flux through the  $22.5^\circ\text{C}$ ,  $15^\circ\text{C}$  and  $5^\circ\text{C}$  isotherms due to numerical

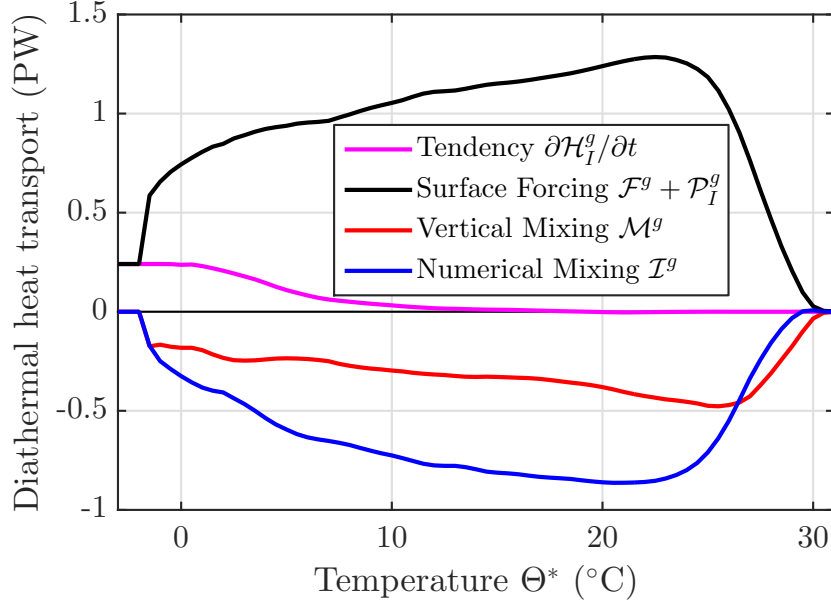


**Figure 2.** Globally-integrated internal heat content budget [Eq. (9)] for ACCESS-OM2-025. Shown are the total heat transport into all water warmer than a given temperature  $\Theta$  due to surface forcing  $\mathcal{F}^g + \mathcal{P}_I^g$  (black); explicitly-parameterized vertical mixing  $\mathcal{M}^g$  (red); and numerical mixing  $\mathcal{I}^g$  (blue); as well as the internal heat content tendency  $\partial\mathcal{H}_I^g/\partial t$  (magenta). The global metric  $\mathcal{I}_{\text{net}}$  discussed in Section 2.6 and listed in Table 1 is the area above the curve of  $\mathcal{I}^g$ .

mixing averaged over 10 years in ACCESS-OM2-025. The flux has substantial spatial variability with hot-spots in the eddying WBCs and the ACC, near the continental shelves and slopes, and in the tropical thermocline. The flux is dominantly down-gradient over all three isotherms, as expected given the flux limiters on the advection scheme. However, there are notable regions with up-gradient fluxes, which are discussed in Appendix A (Section A.3).

#### 4.1 Warm temperatures

At warm temperatures (e.g. 22.5°C, Fig. 3a) numerical mixing is particularly strong and extensive in the thermocline of the central and eastern tropical Pacific and the tropical Atlantic. The most intense fluxes are located east of the Galapagos in the Pacific and along the western boundary in the Atlantic. In both basins there are tongues of high mixing on either side of the Equator within the thermocline. These regions are characterized by strong grid-scale vertical and horizontal temperature gradients (Fig. 4c,e) which numerical mixing acts to smooth (creating large down-gradient heat fluxes). Horizontal grid-scale velocity differences are also large, reaching root-mean-square values of 0.05 m s<sup>-1</sup> in these regions (Fig. 4a). This grid-scale variability in the horizontal velocity may be a major driver of the numerical mixing diagnosed in this region. The reason is that noise in the horizontal velocity translates into a noisy vertical velocity through continuity, and thus to noisy vertical advection across the thermocline (Ilicak et al., 2012).

Grid-scale noise in the horizontal velocity field can arise from numerical instabilities of the centered second-order momentum advection scheme (Leonard, 1984), momentum advection-diffusion (Bryan, Manabe, & Pacanowski, 1975) or physical instabilities such as baroclinic instability acting near the grid scale (particularly at eddy-permitting resolution). Ilicak et al. (2012) proposed the grid Reynolds number as a proxy for the

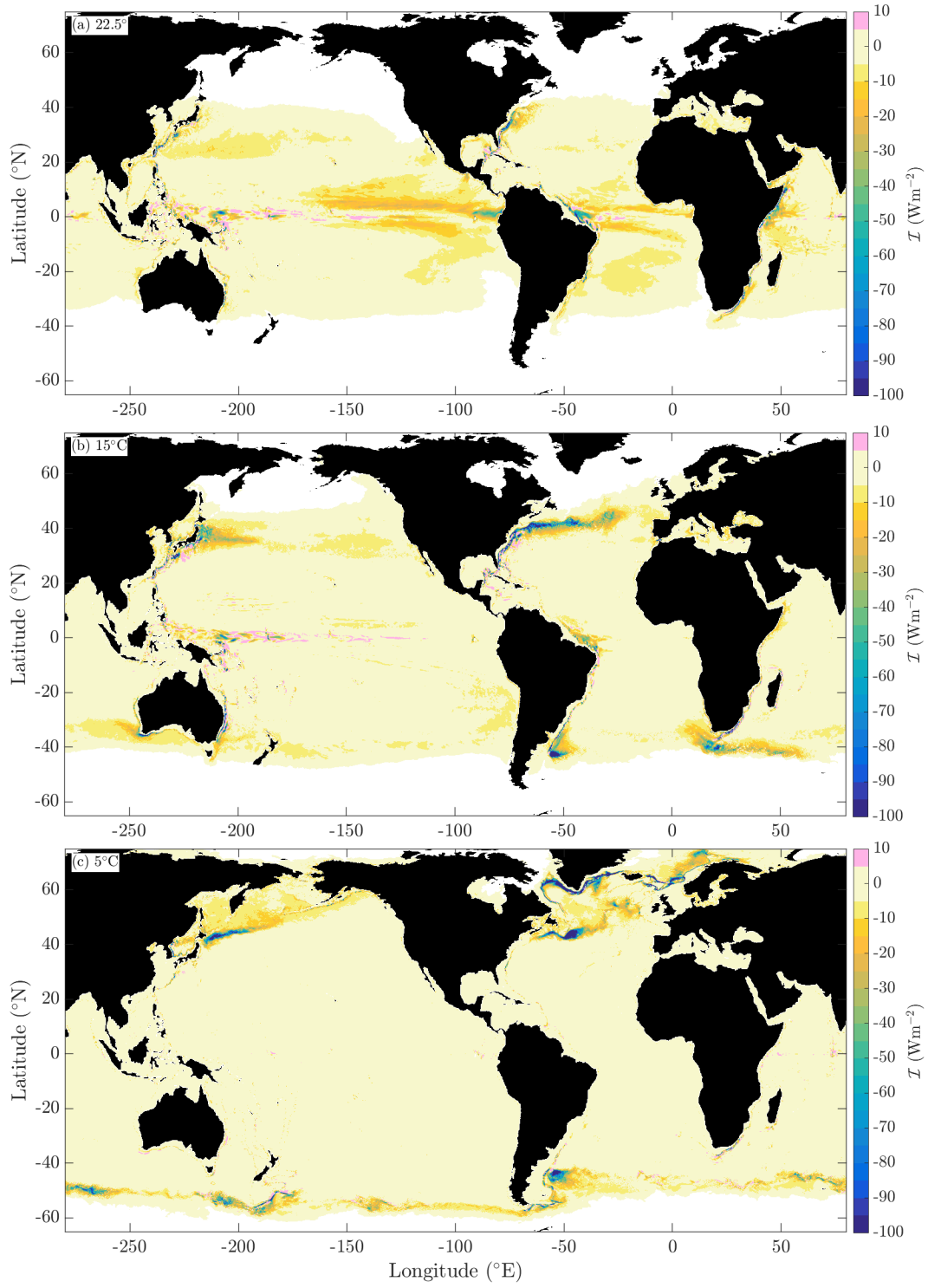


**Figure 3.** Heat flux due to numerical mixing,  $\mathcal{I}$  ( $\text{W m}^{-2}$ ), through the (a) 22.5°C; (b) 15°C and (c) 5°C isotherms in ACCESS-OM2-025. The color interval is 5  $\text{W m}^{-2}$  and positive up-gradient fluxes greater than 5  $\text{W m}^{-2}$  are shown in pink.

levels of spurious mixing, with sufficiently large viscosity needed to damp grid-scale horizontal velocity variability, reduce noisy vertical velocities and thus render small spurious mixing. However, when calculated using the square-root of the total kinetic energy (divided by  $\rho_0$ ) as the velocity scale, we found that spatial variability in the biharmonic grid Reynolds number was not representative of the spatial structure in numerical mixing (not shown). This may be because the grid Reynolds number does not include any measure of temperature variance on which numerical mixing depends, or that the total kinetic energy is not as relevant a velocity scale for numerical mixing as a measure of the grid-scale horizontal velocity variance. Hence, here we choose to focus more directly on the grid-scale horizontal velocity and temperature variances themselves (e.g. Fig. 4).

Numerical mixing along the Equator in the Pacific is strongest east of the Galapagos where the thermocline is particularly sharp and lies close to the surface (Fig. 5a). This region is correlated with strong horizontal grid-scale temperature differences (Fig. 5d). Weaker but more extensive levels of numerical mixing reaching  $15 \text{ W m}^{-2}$  are also found in the upper 100 m (generally above the thermocline, Fig. 5a). Some of this numerical mixing occurs in the vicinity of the highly-sheared upper Equatorial Undercurrent coinciding with the peak in explicitly-parameterized vertical mixing associated with shear instability (compare Figs. 5a,b, also see HZE19). This region is characterized by enhanced grid-scale horizontal velocity gradients (Figs. 5c, 4a) likely associated with eddy flows such as Tropical Instability Waves (TIWs). TIWs are known to create strong fronts and both temperature and velocity variability in models and observations that influences turbulent mixing in the region (e.g. Warner et al., 2018). It is conspicuous that numerical mixing is restricted to isotherms that generally lie in the upper 100 m where grid-scale horizontal velocity differences (and TIW variability) is strongest and above the strong vertical temperature gradients in the thermocline. This pattern suggests that numerical mixing is unlikely to be associated with exclusively vertical advective processes. Note also that the numerical mixing in the equatorial regions exhibits a seasonal cycle consistent with the seasonal cycle in equatorial trade winds, current shear and Tropical Instability Waves (e.g. see Fig. 11b of HZE19). While further study is required to evaluate the specific causes of numerical mixing in this region, some insight will be provided by parameter sensitivity tests in Section 5.

While we cannot isolate the diapycnal and isopycnal components of numerical mixing, the dominance of density variations by temperature in the tropics suggests that much of the numerical mixing in this region is diapycnal. This numerical mixing contributes to the too-diffuse vertical temperature gradients that characterize many models and have been implicated in SST biases such as the equatorial cold tongue bias or eastern upwelling region warm biases in global climate models (e.g. Richter, 2015, also see Section 5.2).

## 4.2 Cold temperatures

At colder temperatures (e.g.  $15^\circ\text{C}$  and  $5^\circ\text{C}$ , Figs. 3b,c) numerical mixing is most prominent in the eddy-rich WBCs and the ACC. At  $15^\circ\text{C}$  the numerical mixing in the North Atlantic stretching along the length of the Gulf Stream and its extension across the basin is particularly prominent. These regions are characterized by large grid-scale temperature and horizontal velocity differences (Fig. 4b,d). In contrast, the vertical grid-scale temperature differences in these regions do not stand out (Fig. 4f). Thus, numerical mixing in these regions is likely associated with lateral mesoscale eddy stirring that creates strong horizontal temperature gradients near the grid-scale that are subsequently smoothed by the advection operator. This process mimics the real ocean equivalent of a downscale cascade of temperature variance along neutral directions by mesoscale stirring towards its ultimate dissipation at small scales through irreversible mixing (e.g. McDougall, Groeskamp, & Griffies, 2014; Smith & Ferrari, 2009). In the model, where there is no explicit lateral diffusion, the numerical mixing is presumably acting as a substitute for small-scale diffusion by dissipating the gradients near the grid-scale.



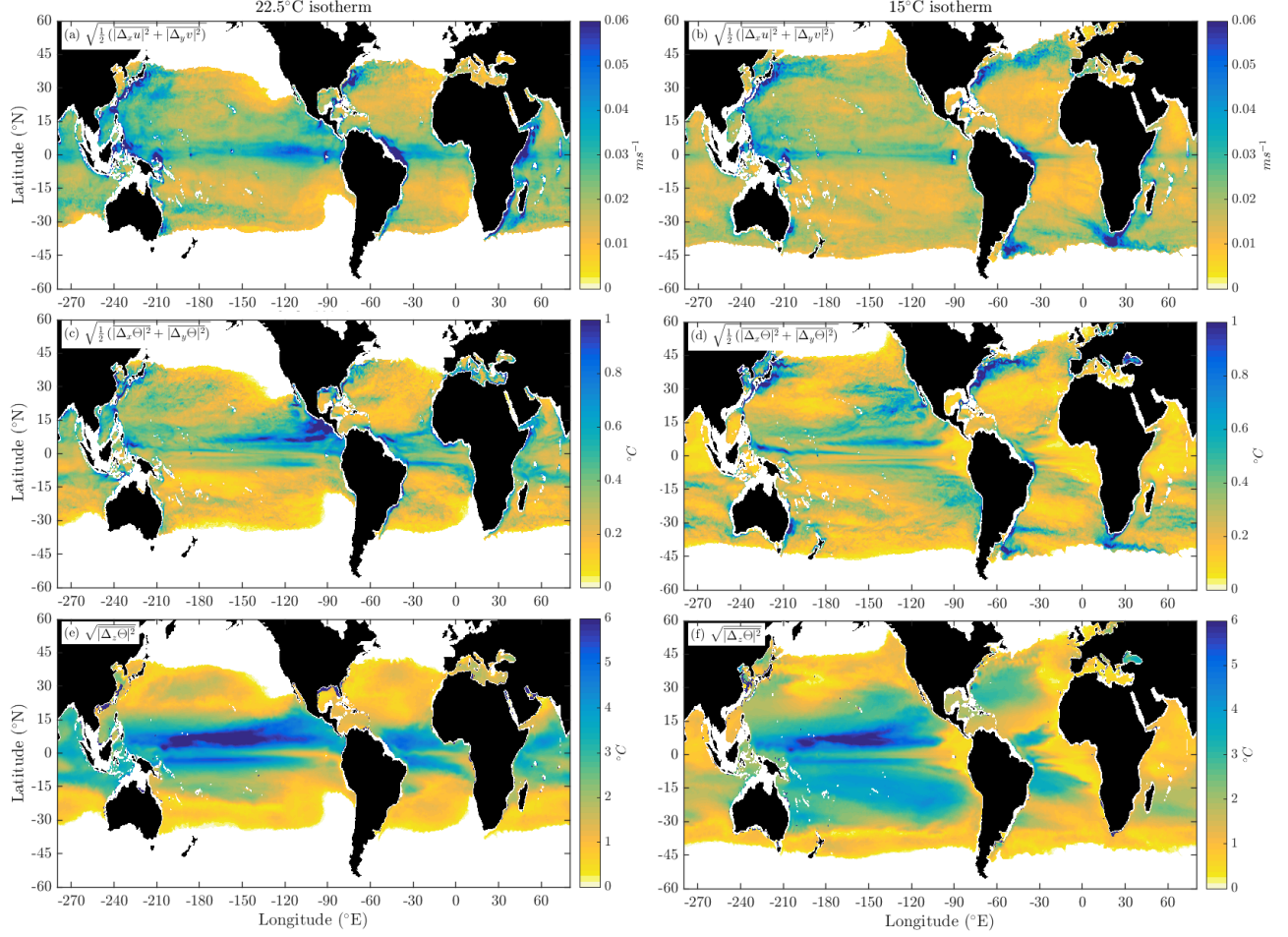


**Figure 4.** Root-mean-square (a,b) horizontal velocity grid cell differences, (c,d) horizontal temperature grid cell differences and (e,f) vertical temperature grid cell differences on the (a,c,e) 22.5°C and (b,d,f) 15°C isotherms from ACCESS-OM2-025. These quantities are calculated by taking the square of the difference in the specified direction ( $\Delta_x$ ,  $\Delta_y$  or  $\Delta_z$ ) of the specified quantity ( $u$ ,  $v$  or  $\Theta$ ) at each time step, time-averaging over a month, interpolating onto the monthly-averaged isotherm and then taking the long-term time-average and square-root. Note that the colormaps saturate at high values.

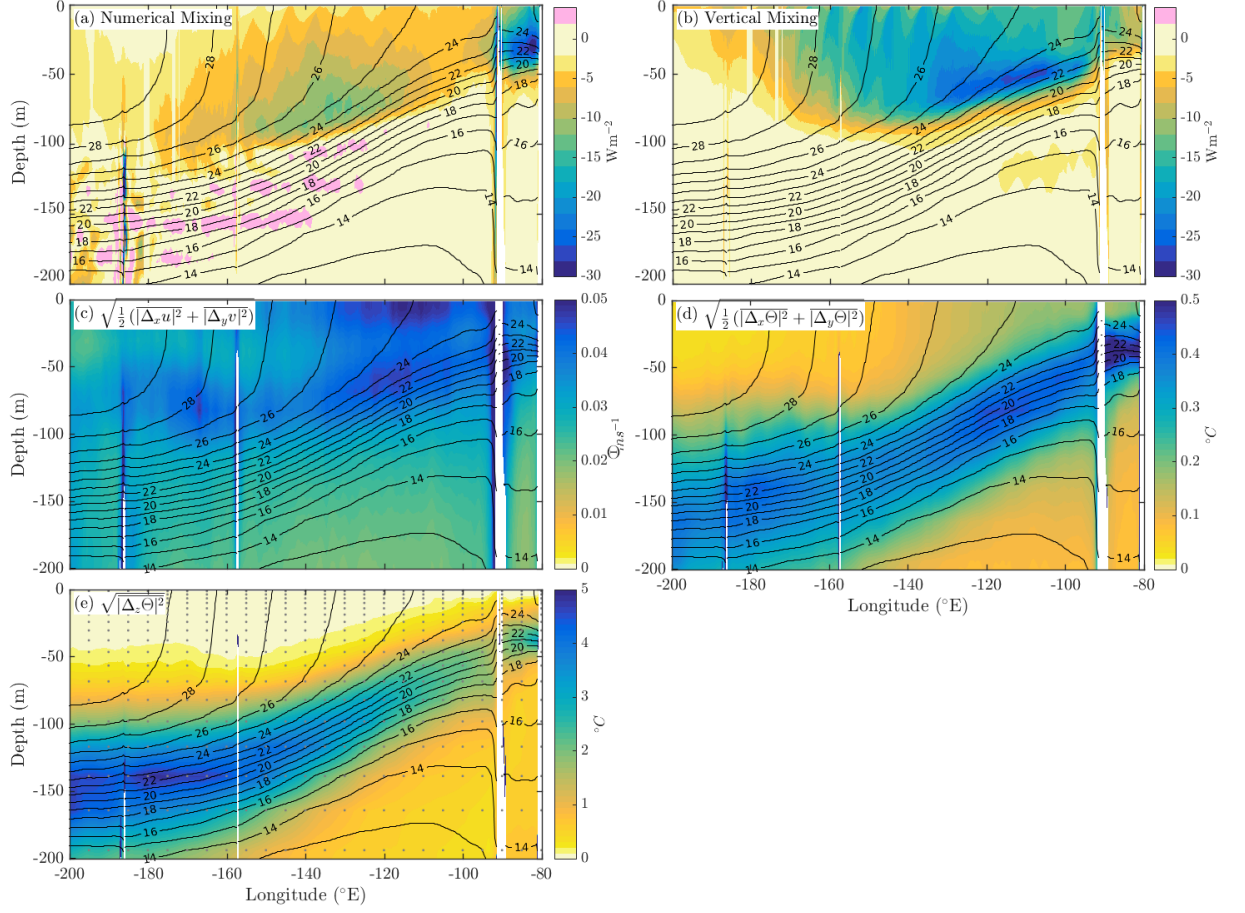


**Figure 5.** Longitude-depth slices between  $\pm 2^\circ$  of the Equator in the eastern Pacific of the (a) numerical mixing and (b) vertical mixing heat flux across isotherms from ACCESS-OM2-025. The heat flux is averaged in temperature coordinates and then remapped to depth using the annual-mean isotherm depths. The color interval is  $2 \text{ W m}^{-2}$  and positive up-gradient fluxes greater than  $2 \text{ W m}^{-2}$  are shown in pink. Root-mean-square (c) horizontal velocity grid cell differences, (d) horizontal temperature grid cell differences and (e) vertical temperature grid cell differences. The gray dots in panel e show the vertical grid locations of the KDS50 grid used in ACCESS-OM2-025.



In addition to the eddying WBCs, there are some contributions from topographic hot spots around the continental shelves (e.g. around Australia in Fig. 3b). At warmer temperatures these regions make a minor contribution to the global transport. However, at 5°C there are large fluxes around the continental shelves in the high-latitude North Atlantic (Fig. 3c). These continental slope regions are once again characterized by strong grid-scale temperature and horizontal velocity differences (e.g. Fig. 4b,d).

## 5 Sensitivity to model parameters

In this section we examine the sensitivity of numerical mixing to various model parameters. The global-average diathermal heat budgets for each configuration are shown together in Fig. 6, with numerical mixing in panels i and j. The globally-integrated summary diagnostic  $\mathcal{I}_{\text{net}}$  discussed in Section 2.6, being the area above the curve of Figs. 6i,j, is listed in Table 1. We will consider the impact of varying explicit neutral physics parameterizations (Section 5.1), background vertical diffusivity (Section 5.2), vertical resolution (Section 5.3), horizontal resolution (Section 5.4) and lateral viscosity (Section 5.5).

Changes in model parameters or resolution can impact the global diathermal heat budget shown in Fig. 6 in a number of interacting ways. For example, changes in explicit mixing parameters alter the temperature structure of the solution. This change in temperature structure can impact on numerical mixing (Fig. 6i,j), for example through reduced gradients for the numerical mixing to act on. Feedbacks then can project onto the physical mixing itself as well as the surface forcing (Fig. 6a,b) through changes in the SST or upper-ocean thermal structure into which those surface fluxes enter. Here we focus on semi-equilibrated simulations meaning that differences measured between simulations are the result of a chain of feedbacks.

### 5.1 Neutral physics

As discussed in Section 4, at cold temperatures numerical mixing is largely associated with the eddying WBCs and ACC (e.g. Fig. 3b,c), where at 1/4° and finer grid spacings large lateral temperature gradients are created by along-isopycnal mesoscale eddy-stirring (e.g. Fig. 4d). Here, it is likely that the diathermal heat flux arising from numerical mixing is linked to isopycnal and lateral processes. In ACCESS-OM2-025 as well as the 1/10° ACCESS-OM2-01 configuration, no explicit parameterization for lateral or neutral mixing are included. This choice, also made for the MOM025 configurations considered by HZE19, was made in order to maximize the preservation of isopycnal tracer gradients at resolved scales, leaving the advection scheme to smooth gradients near the grid scale and thereby allowing the model to make the most of its resolution. Here, we examine the interplay between the numerical and parameterized neutral diffusion by comparing ACCESS-OM2-025 with ACCESS-OM2-025-NG, where both neutral diffusion and the GM eddy-induced advection parameterizations are active, and with ACCESS-OM2-025-N, where only neutral diffusion is active (red lines in Fig. 6b,d,f,h,j).

When neutral diffusion and the GM parameterizations are both turned on, numerical mixing reduces between -1°C and 25°C (compare red solid and red dashed lines in Fig. 6j), with the strongest impact being between -1°C and 15°C where the diathermal heat transport due to parameterized neutral diffusion in ACCESS-OM2-025-NG peaks (dashed red line in Fig. 6h). These changes are largely due to the presence of explicit neutral diffusion, with the presence or absence of the GM scheme having a smaller impact. Both heat fluxes due to neutral diffusion and numerical mixing are slightly enhanced when GM is turned off (compare dotted and dashed red lines in Fig. 6h,j). The replacement of parameterized neutral diffusion with enhanced numerical mixing and vice versa appears relatively benign with respect to the global diathermal heat budget, with only

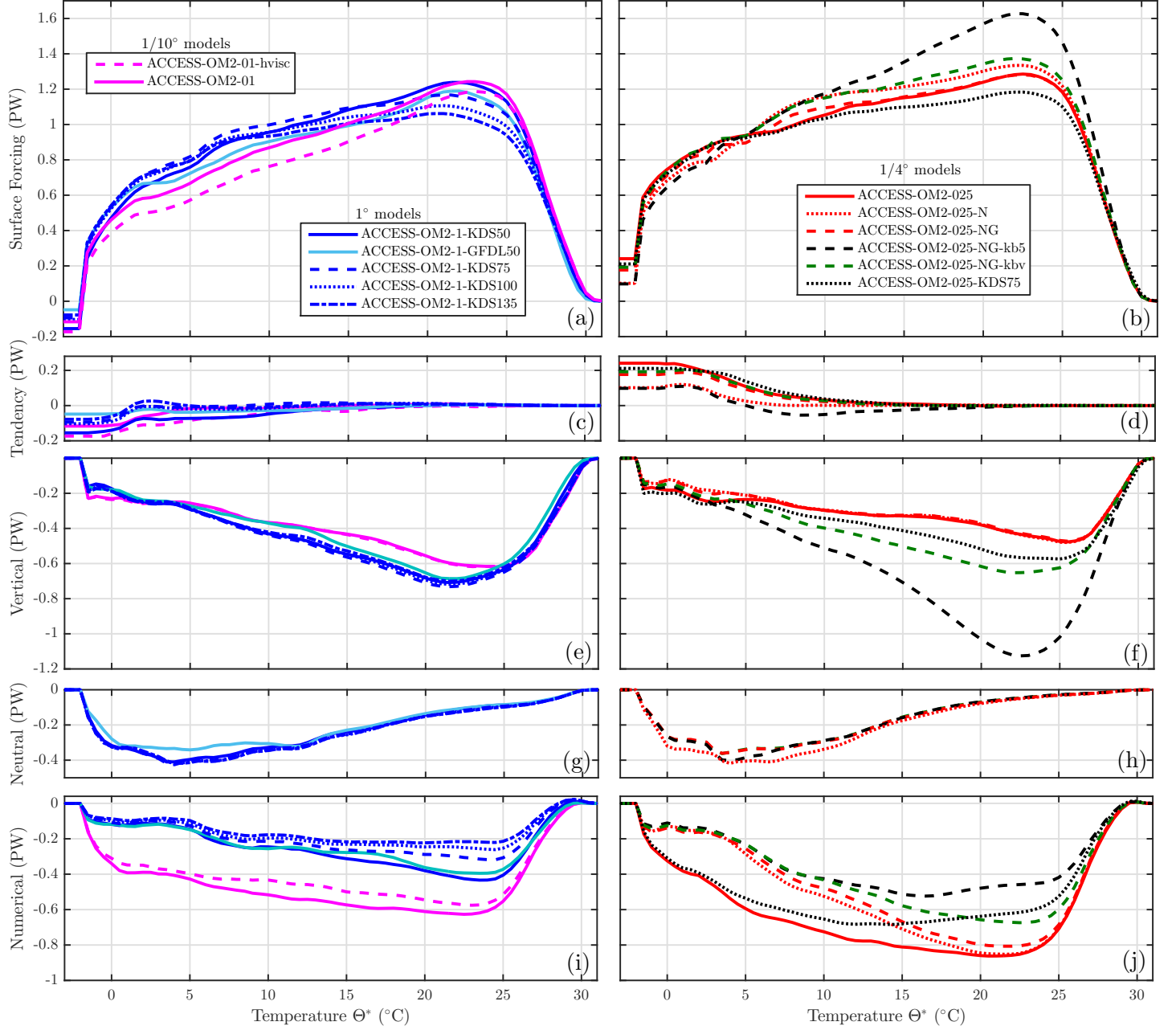


**Figure 6.** The global annually-averaged diathermal heat budget [Eq. (9)] across the suite of model simulations. (a,b) Surface forcing  $\mathcal{F}^g + \mathcal{P}_I^g$ , (c,d) the internal heat content tendency  $\partial \mathcal{H}_I^g / \partial t$ , (e,f) explicitly-parameterized vertical diffusion  $\mathcal{M}^g$ , (g,h, if present) explicitly-parameterized neutral diffusion  $\mathcal{N}^g$  and (i,j) numerical mixing  $\mathcal{I}^g$ . Note that the vertical scale of every panel is the same to facilitate comparison. The global metric  $\mathcal{I}_{\text{net}}$  discussed in Section 2.6 and listed in Table 1 is the area above the curve of  $\mathcal{I}^g$ .

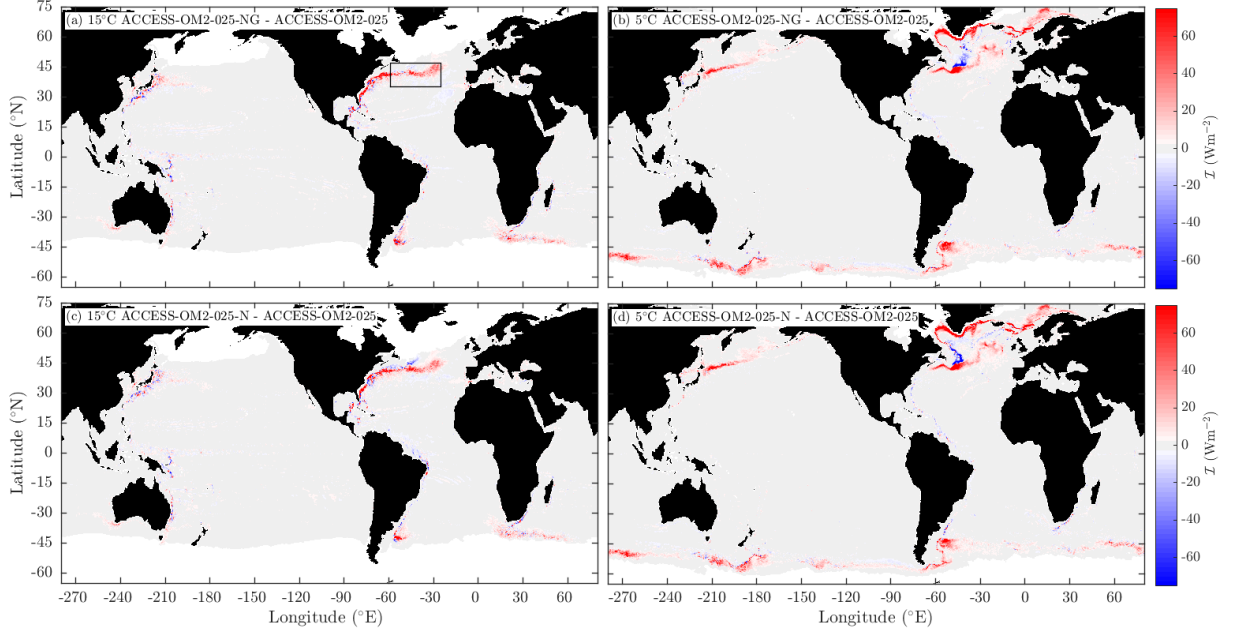


**Figure 7.** Difference in the diathermal heat flux due to numerical mixing through the (a,c) 15°C and (b,d) 5°C isotherms in the (a,b) ACCESS-OM2-025-NG with both neutral diffusion and the GM parameterization and (c,d) ACCESS-OM2-025-N with only neutral diffusion compared with ACCESS-OM2-025 which has neither (the ACCESS-OM2-025 totals are shown in Fig. 3b,c). Red indicates a decrease in the magnitude of down-gradient numerical diffusion when the respective parameterizations are turned on. The black box in panel (a) indicates the Gulf Stream extension region analyzed in Fig. 8.

small changes in the surface forcing, tendency or vertical diffusion terms (compare red solid and dashed lines in Fig. 6b,d,f).

While the neutral diffusivity is scaled by the ratio of the grid spacing and the Rossby radius of deformation (it has values of less than  $20 \text{ m}^2 \text{ s}^{-1}$  in the tropics where the Rossby radius is better resolved, while reaching  $200 \text{ m}^2 \text{ s}^{-1}$  at high-latitudes and over shallow shelves), tests with an older configuration that utilized a constant neutral diffusivity of  $300 \text{ m}^2 \text{ s}^{-1}$  showed only a small further reduction in numerical mixing (not shown). Changes of less than 0.02 PW occurred at temperatures warmer than  $20^\circ\text{C}$ , suggesting again that numerical mixing at warmer temperatures in the tropics is associated with diapycnal, and not isopycnal, processes. Instead, the changes in numerical mixing occur nearly exclusively in the WBCs, ACC and high-latitude continental shelves/slopes where eddy-variability dominates (Fig. 7). While in most of these areas numerical mixing shows an overall reduction when neutral diffusion is introduced, there are also some localized regions where numerical mixing is increased due to shifts in the location of mean currents and eddy pathways (e.g. north of the Gulf Stream in Fig. 7b,d).

As a representative region, we examine changes in the Gulf Stream extension in more detail (Fig. 8). In this region there is a broad reduction of numerical mixing in ACCESS-OM2-025-NG and ACCESS-OM2-025-N across the  $2\text{--}20^\circ\text{C}$  range, peaking at a  $\sim 40\%$  reduction near  $10^\circ\text{C}$  (Fig. 8a). This reduction in numerical mixing is associated with a reduction in Eddy Kinetic Energy (EKE), resolved eddy-driven stirring and therefore horizontal grid-scale velocity and temperature differences (Fig. 8b-d). Changes in vertical grid-scale temperature differences are less coherent (Fig. 8e). While the GM scheme

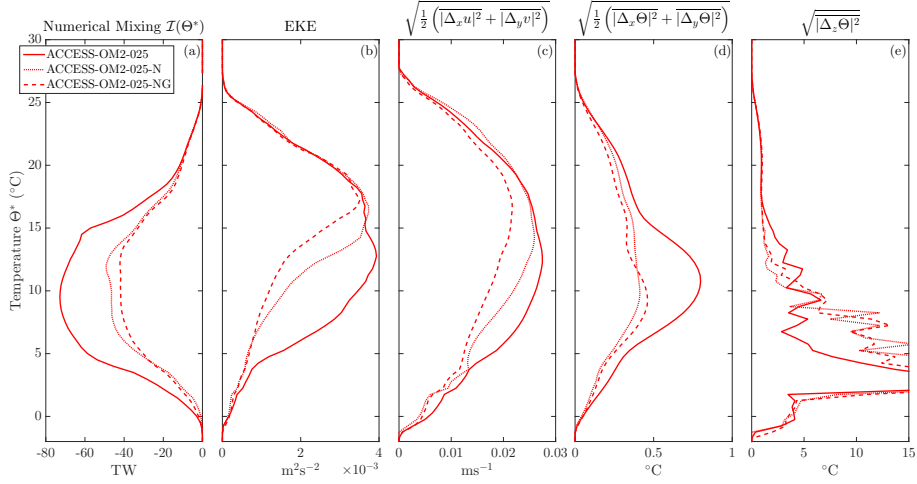


**Figure 8.** Differences in numerical mixing and grid-scale horizontal velocity and temperature differences in the Gulf Stream extension ( $59^{\circ}\text{W}$ - $25^{\circ}\text{W}$ ,  $35^{\circ}\text{N}$ - $47^{\circ}\text{N}$ , black box in Fig. 7a). (a) Diathermal heat transport due to numerical mixing  $\mathcal{I}(\Theta)$ , (b) sub-monthly EKE and root-mean-square grid-scale (c) horizontal velocity, (d) horizontal temperature and (e) vertical temperature differences. The quantities in panels (b)-(e) are interpolated onto isotherms using monthly-averaged temperature and then spatially and temporally averaged.

has a larger impact on horizontal grid-scale velocity differences (Fig. 8c), neutral diffusion has the dominant impact on horizontal grid-scale temperature differences. These changes in horizontal grid-scale temperature differences appear to drive the majority of the changes in numerical mixing (Fig. 8a). These results support the conclusion that in active mesoscale eddying regions the dominant driver of numerical mixing is grid-scale noise in the horizontal velocity and temperature fields (e.g. Ilicak et al., 2012). Neutral diffusion reduces numerical mixing by smoothing horizontal grid-scale temperature differences, while the GM scheme drives a small further reduction in numerical mixing by reducing horizontal velocity variability. However, while numerical mixing is reduced when these parameterizations are turned on, other changes in the simulations, such as reduced eddy activity, emphasize that it remains an open question as to whether it is better to dissipate grid-scale temperature gradients through numerical or explicit mixing.

## 5.2 Background vertical diffusivity

As discussed in HZE19, there is an interplay between the explicit vertical mixing and the numerical mixing. When explicit vertical mixing is increased, small-scale vertical gradients in temperature are decreased and therefore numerical mixing, if linked with vertical advective processes, will decrease (in addition to secondary feedbacks to the circulation). This mechanism is evident when comparing the ACCESS-OM2-025-NG configurations which differ only in their background vertical diffusivity, particularly at temperatures above  $10^{\circ}\text{C}$  (compare red, black and green dashed lines in Fig. 6b,d,f,j). Increasing the background vertical diffusivity from 0 to  $10^{-5} \text{ m}^2 \text{ s}^{-1}$ , a typical background value used in many climate models, more than doubles the peak diathermal heat transport due to vertical mixing between  $20^{\circ}\text{C}$  and  $25^{\circ}\text{C}$ . However, the subsequent change in the total diathermal heat transport (that which balances the surface forcing, Fig. 6b) is less, due to compensation by changes in numerical mixing (Fig. 6j). Numerical mixing is decreased by approximately a factor of 2 when the  $10^{-5} \text{ m}^2 \text{ s}^{-1}$  background diffusivity is turned on (compare black and red dashed lines in Fig. 6j).

On the 22.5°C isotherm, near the peak of the diathermal heat transport, the changes in numerical mixing occur primarily in the tropical thermocline (Fig. 9a), particularly in the eastern Pacific and Atlantic where the thermocline is sharp and background diffusion can drive large diathermal heat fluxes (e.g. see HZE19, their Fig. 4b). Given that temperature dominates density variability in the tropics, the changes in numerical mixing as the vertical diffusivity is changed supports the conclusion that the numerical mixing in these regions is diapycnal. There are also some changes in the mid-latitude interior where background diffusion is replaced by numerical mixing when the background diffusivity is set to zero. However, there is little consistent change in numerical mixing in the WBCs or continental slopes and shelves, supporting the conclusion made in the previous section that numerical mixing here is associated with lateral rather than vertical processes. Consequently, at cold temperatures the dependence of numerical mixing on the background vertical diffusivity is weak despite significant changes in the diathermal heat transport due to vertical mixing (compare dashed lines in Fig. 6f,j).

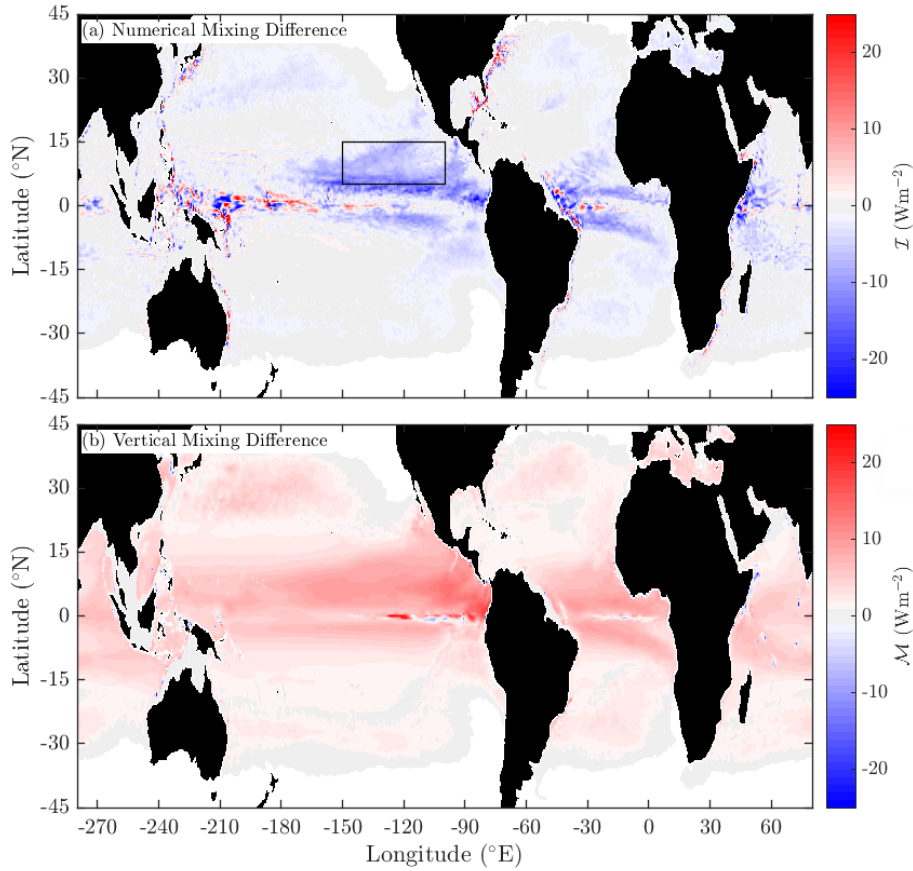


**Figure 9.** The difference between the heat flux across the 22.5°C isotherm due to (a) numerical mixing and (b) vertical mixing between the ACCESS-OM2-025-NG configuration with no background vertical diffusivity and the ACCESS-OM2-025-NG-kb5 configuration with a  $10^{-5} \text{ m}^2 \text{ s}^{-1}$  background vertical diffusivity. Both numerical and vertical mixing fluxes are negative (down-gradient), meaning that the blue regions in panel (a) signal an increase in the strength of numerical mixing in ACCESS-OM2-025-NG compared to ACCESS-OM2-NG-kb5 while the red regions in panel (b) signal a decrease in the strength of vertical mixing in ACCESS-OM2-025-NG compared to ACCESS-OM2-NG-kb5. The black box in panel (a) indicates the region analyzed in Fig. 10.

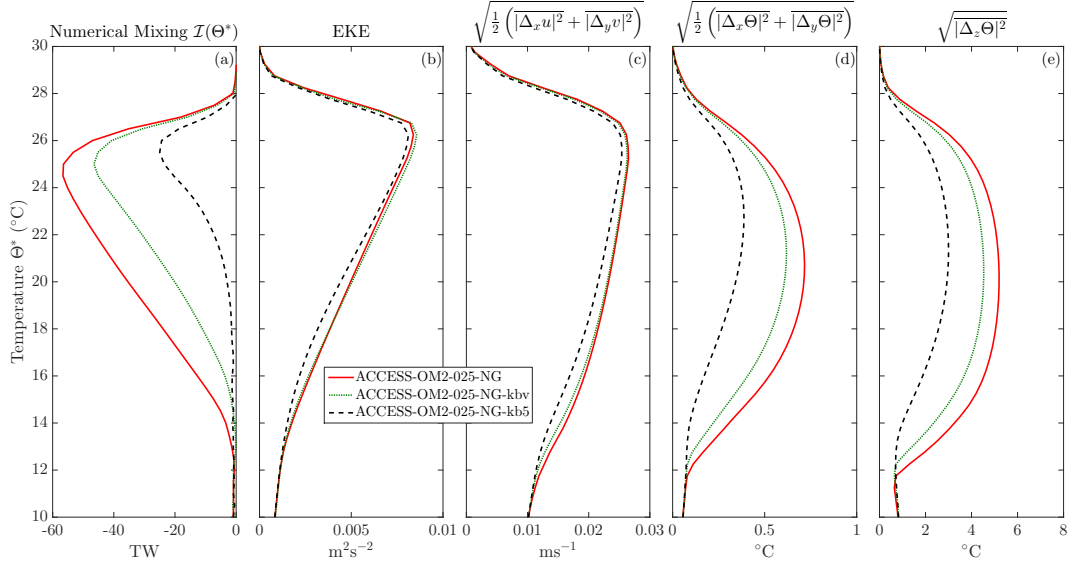


**Figure 10.** Analysis of the sensitivity of numerical mixing and grid-scale temperature and horizontal velocity differences to the background vertical diffusivity in the Eastern Tropical Pacific (150°W-100°W, 5°N-15°N, black box in Fig. 9a). ACCESS-OM2-025-NG has no background vertical diffusivity, ACCESS-OM2-025-NG-kb5 has a background vertical diffusivity of  $10^{-5} \text{ m}^2 \text{ s}^{-1}$  and ACCESS-OM2-025-NG-kbv has a latitudinally-dependent background vertical diffusivity of between  $1 \times 10^{-6} \text{ m}^2 \text{ s}^{-1}$  and  $3 \times 10^{-6} \text{ m}^2 \text{ s}^{-1}$  in this region. (a) Diathermal heat transport due to numerical mixing  $\mathcal{I}(\Theta)$ , (b) sub-monthly EKE and root-mean-square grid-scale (c) horizontal velocity, (d) horizontal temperature and (e) vertical temperature differences. The quantities in panels (b)-(e) are interpolated onto isotherms using monthly-averaged temperature and then spatially and temporally averaged.

Focusing on a region in the Eastern Tropical Pacific (black box in Fig. 9a), the background diffusivity has little influence on horizontal velocity variability or grid-scale differences (Fig. 10b,c). However, the expected reduction in grid-scale vertical temperature differences when the background diffusivity is increased is also accompanied by a similar factor reduction in horizontal grid-scale temperature differences (Fig. 10d,e). This result suggests that horizontal grid-scale temperature variability is created by small-scale vertical advection of the background vertical temperature gradient. Reducing this background vertical temperature gradient by increasing the vertical diffusivity reduces both horizontal and vertical temperature gradients at the grid-scale, in turn leading to a reduction in numerical mixing (Fig. 10a).

The changes in background diffusivity have an impact on temperature biases in the equatorial Pacific thermocline (Fig. 11a,b,c). ACCESS-OM2-025-NG-kbv, with a background diffusivity of  $10^{-6} \text{ m}^2 \text{ s}^{-1}$  at the Equator, shows a slightly smaller overall bias than the default configuration of ACCESS-OM2-025-NG (no background diffusivity) which has a strong cold bias below the thermocline, suggesting that the larger numerical mixing in ACCESS-OM2-025-NG does not compensate for reduced vertical mixing (i.e. a small explicit background vertical diffusivity is needed to reduce equatorial biases). In contrast, ACCESS-OM2-025-NG-kb5 (Fig. 11c) is too warm nearly everywhere.



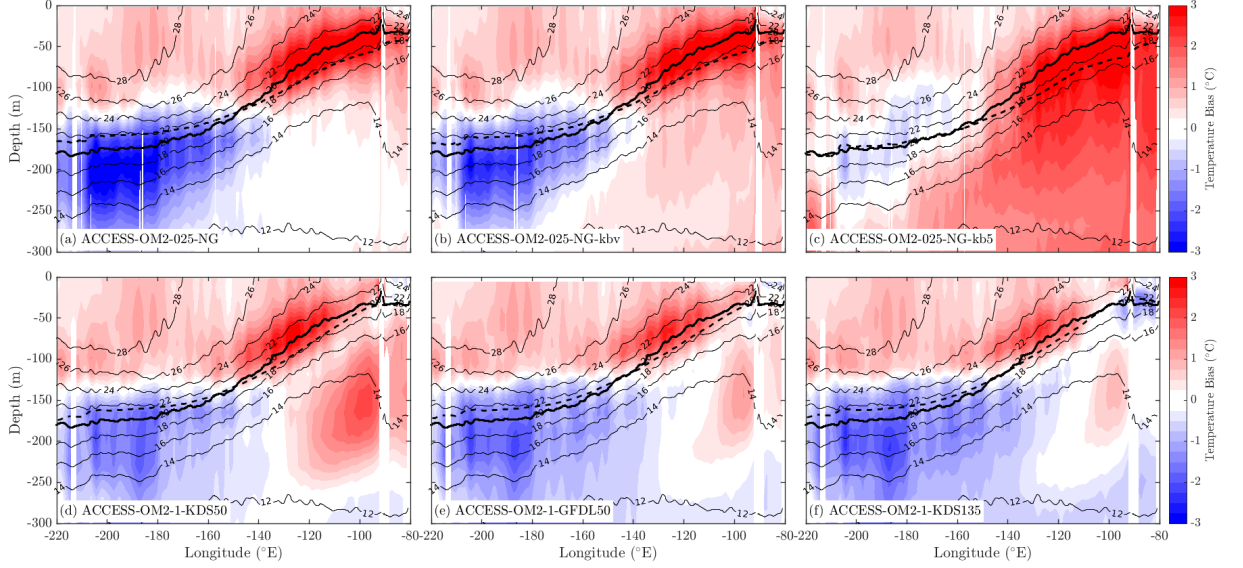


**Figure 11.** Equatorial Pacific depth-longitude temperature bias plots compared to WOA13 for (a-c) three ACCESS-OM2-025-NG configurations with differing background vertical diffusivity and (d-f) three ACCESS-OM2-1 configurations with differing vertical resolution. ACCESS-OM2-025-NG uses no background vertical diffusivity, ACCESS-OM2-025-NG-kb5 uses a background diffusivity of  $10^{-5} \text{ m}^2 \text{ s}^{-1}$  and ACCESS-OM2-025-NG-kbv and the ACCESS-OM2-1 configurations use a background diffusivity of  $10^{-6} \text{ m}^2 \text{ s}^{-1}$  on the Equator. The contours show the WOA13 isotherms with the  $20^\circ\text{C}$  isotherm in a thicker line. The thick dashed line is the position of the modeled  $20^\circ\text{C}$  isotherm.

### 5.3 Vertical resolution

Numerical mixing is also sensitive to the vertical resolution, here examined using a set of ACCESS-OM2-1 simulations. Most of the configurations in this article use the Stewart et al. (2017, denoted KDS) vertical levels scheme which has fine grid spacing in the upper ocean (nearing 1–2 m near the surface, colored lines in Fig. 12) in order to better resolve the vertical structure of baroclinic modes in shallow regions. We also consider a configuration with the 50 level grid used in the ocean component of the GFDL CM2.5 climate model (GFDL50), which has 10 m vertical grid spacing in the upper 200 m (black line in Fig. 12).

The changes in vertical grid spacing have an impact on numerical mixing at most temperatures, with the largest changes between  $15^\circ\text{C}$  and  $27^\circ\text{C}$  (compare blue lines in Fig. 6i). As for the background diffusivity, the dominant changes occur in the equatorial regions where the vertical temperature stratification is largest. An equatorial Pacific longitude-depth slice for each configuration is shown in Fig. 13. In general, as the number of grid levels increases, the numerical mixing reduces. However, the placement of the levels also makes a difference. The KDS grid has a much finer vertical grid spacing near the surface (2.3 m in KDS50 and 1.1 m in KDS75 compared to 10 m in GFDL50, Fig. 12), meaning that the sharp vertical gradients in the far eastern Pacific shallower than 50 m depth are better resolved by the KDS50 grid. Numerical mixing in ACCESS-OM2-1-GFDL50 here is much larger (compare Figs. 13a and 13b east of  $-100^\circ\text{E}$ ). However, between 50 m and 250 m depth the GFDL50 grid has a finer vertical grid spacing than KDS50 (compare black and blue lines in Fig. 12) and so numerical mixing is lower in GFDL50 (compare Figs. 13a and 13b in the central Pacific). This depth range cor-



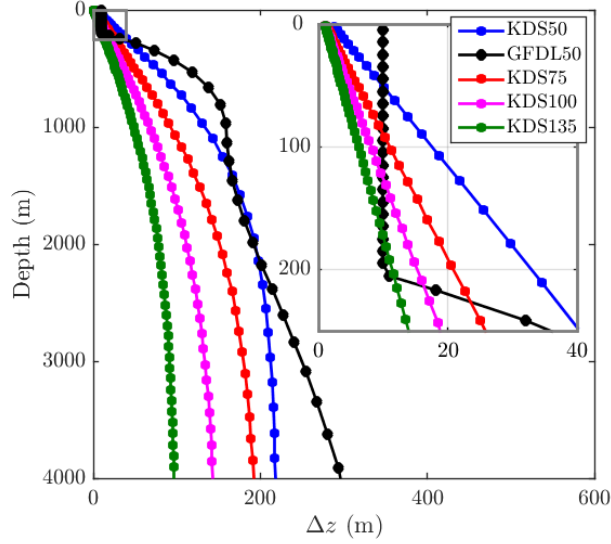


**Figure 12.** The vertical grid spacing  $\Delta z$  as a function of depth for the five vertical grids used in this study. The inset shows a zoom on the upper 250m (gray box).

responds to the thermocline where vertical temperature gradients are largest throughout most of the ocean, and so globally numerical mixing is slightly lower in ACCESS-OM2-1-GFDL50 than in ACCESS-OM2-1-KDS50 above  $\sim 13^\circ\text{C}$  (compare light and dark blue lines in Fig. 6i).

It is interesting to note that numerical mixing at cold temperatures is also sensitive to the vertical resolution, despite being insensitive to the background vertical diffusivity. These changes may be linked to the interplay between horizontal and vertical grid-scale temperature gradients in the presence of grid-scale horizontal velocity variability. However, we note that ACCESS-OM2-1 does not resolve eddy-variability.

In the KDS50 configuration there are some weak apparent up-gradient numerical mixing fluxes in the lower portion of the thermocline in the western and central Pacific (pink in Fig. 13). As discussed in more detail in Appendix A, the use of flux limiters on the MDPPM advection scheme should maintain monotonicity in the advected tracer distribution and prevent up-gradient fluxes, suggesting that these apparent up-gradient fluxes may arise from limitations in our diagnostic method. These equatorial up-gradient fluxes are in a region where KDS50 has particularly coarse grid spacing - with only 4 vertical levels between 100 m and 200 m (see dots in Fig. 13a). The presence of a large number of isotherms within each single model vertical grid cell suggests that our method for quantifying numerical mixing may be sensitive to small vertical isotherm movements in this region (however, we note that for a given isotherm our method is not sensitive to the temperature binning resolution, here  $0.5^\circ\text{C}$ , as all quantities are integrated over all temperature bins warmer than a given isotherm, see also Appendix A). These weak up-gradient fluxes are present in all simulations that use the KDS50 grid (e.g. ACCESS-OM2-025, Figs. 3a,b and Fig. 5a) but not in configurations using the GFDL50 grid which has a finer grid spacing in this region (e.g. Fig. 13b).

The default time step in ACCESS-OM2-1 is 1.5 hours. However, using this time step apparent up-gradient fluxes of up to  $5 \text{ W m}^{-2}$  appear at the surface at warmer temperatures in the western Pacific in the KDS configurations where the grid spacing is very fine (not shown). Reducing the time step to 20 minutes for the diagnostic accumulation period (as used for all the ACCESS-OM2-1 simulations presented here) removes the ma-

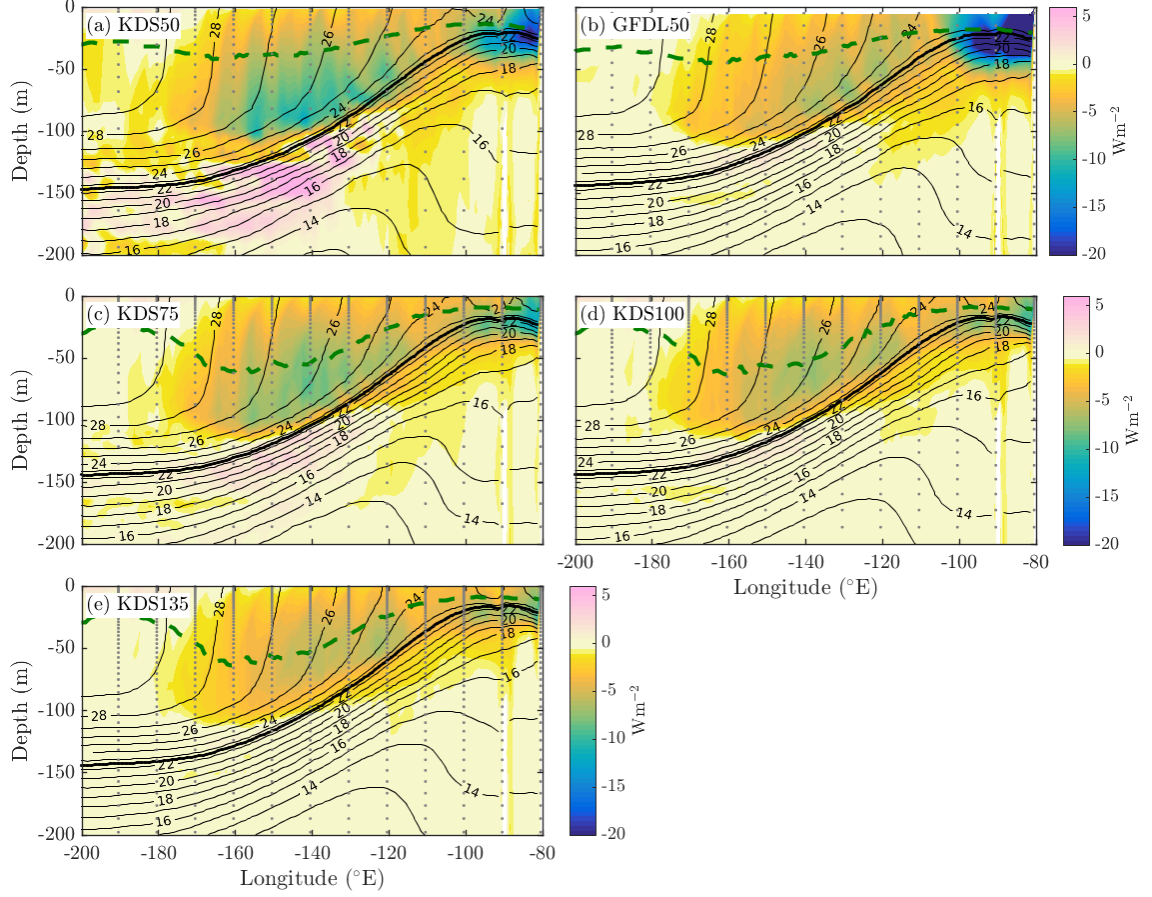


**Figure 13.** Equatorial longitude-depth slices of the numerical mixing heat flux across isotherms averaged within  $\pm 2^\circ$  of the Equator in the ACCESS-OM2 1-degree runs from the coarse (a) KDS50 and (b) GFDL50 configurations to the fine (e) KDS135. The heat flux is averaged in temperature coordinates and then remapped to depth using the annual-mean isotherm depths. Positive up-gradient fluxes are shown in pink shades. The green dashed line indicates the mixed layer depth determined from a  $0.032 \text{ kg m}^{-3}$  density criterion and the gray dots plotted every  $10^\circ$  longitude indicate the vertical grid level locations.

jority of these apparent up-gradient fluxes. A comparison of the terms in the internal heat content budget between the fast and slow time step cases suggests that this apparent up-gradient mixing is linked to an underestimation of the transport of heat into the warmest temperatures classes from surface forcing (not shown). This under-estimation suggests that the rapid changes in near-surface stratification and solar penetrative heating over the diurnal cycle at time scales comparable to the 1.5 hour time step cannot be properly captured by our online diagnostic binning (possibly because of the temporal discretization of the surface forcing and mixing flux convergence binned as discussed in Appendix A, Section A.2). Note that apart from this dependence in ACCESS-OM2-1 we found little dependence of numerical mixing on time step. For example, ACCESS-OM2-025 simulations performed with the default time step of 1350 seconds and 675 seconds showed little difference in numerical mixing metrics (this is reassuring as the time step is often changed during model spin-up to maintain stability).

Unlike the impact of a changing background vertical diffusivity, the changes in numerical mixing with vertical grid spacing do not appear to be compensated by changes in either vertical or neutral diffusion (Fig. 6e,g). Instead, the reduction in numerical mixing results in a change in the surface temperature structure and surface fluxes such that the net diathermal heat transport is altered (blue lines in Fig. 6a). The changes in vertical grid spacing impact the temperature structure in the equatorial Pacific. Finer grids reduce the consistent warm biases at depth in the eastern Pacific by sharpening the thermocline, although at the cost of a slight cold bias in the upper eastern Pacific and a slightly increased cold bias in the deep western Pacific in ACCESS-OM2-1-KDS135 (compare Fig. 11d-f). These results highlight the need to consider the interplay between vertical resolution, vertical background diffusivity and numerical mixing together when making parameter choices. We also see differences at higher latitudes and colder temperatures (Fig. 6i), where Stewart and Hogg (2019) showed that surface fluxes and ocean heat uptake were sensitive to the vertical resolution near the surface.

#### 5.4 Horizontal resolution

Three different horizontal grid spacings have been considered in this study;  $1^\circ$  - where eddy affects outside the tropics are largely parameterized,  $1/4^\circ$  - an “eddy-permitting” resolution where mesoscale eddies outside the tropics are marginally resolved and  $1/10^\circ$  - an “eddy-active” simulation where mesoscale eddies are captured away from the high-latitudes and shallow continental shelves (Hallberg, 2013). In general, comparisons across the model suite shown in Fig. 6i,j or quantified by  $\mathcal{I}_{\text{net}}$  in Table 1 suggest that numerical mixing is strongest at  $1/4^\circ$ , somewhat weaker at  $1/10^\circ$  and weakest at  $1^\circ$ . However, comparisons of numerical mixing across standard configurations at these three horizontal resolutions is complicated by differences in explicit mixing coefficients (these choices are often made, at least in part, for reasons to do with numerical mixing). Here we compare two sets of configurations: ACCESS-OM2-1-KDS50 with ACCESS-OM2-025-NG-kbv and ACCESS-OM2-01 with ACCESS-OM2-025-KDS75 (Fig. 14), that are as close as possible in terms of explicit mixing parameters. These comparisons aim to draw some broad conclusions about changes in numerical mixing with horizontal resolution.

ACCESS-OM2-1-KDS50 and ACCESS-OM2-025-NG-kbv share the same vertical grid and vertical mixing schemes, but differ with respect to neutral diffusion. ACCESS-OM2-025-NG-kbv has a weaker, grid-scale dependent neutral diffusion coefficient with maximum  $200 \text{ m}^2 \text{ s}^{-1}$  compared with the constant value of  $600 \text{ m}^2 \text{ s}^{-1}$  in ACCESS-OM2-1-KDS50. Note, however, that the diathermal heat transport due to neutral diffusion in the two configurations is similar (Fig. 6g,h) suggesting that the enhanced creation of isopycnal temperature variance at  $1/4^\circ$  compensates for the weaker diffusion coefficient to first order. ACCESS-OM2-1-KDS50 has stronger explicit (vertical plus neutral) mixing, and weaker numerical mixing, across most of the temperature range (compare blue and black dashed lines in Fig. 14b,c). While a small portion of this difference may be due to the

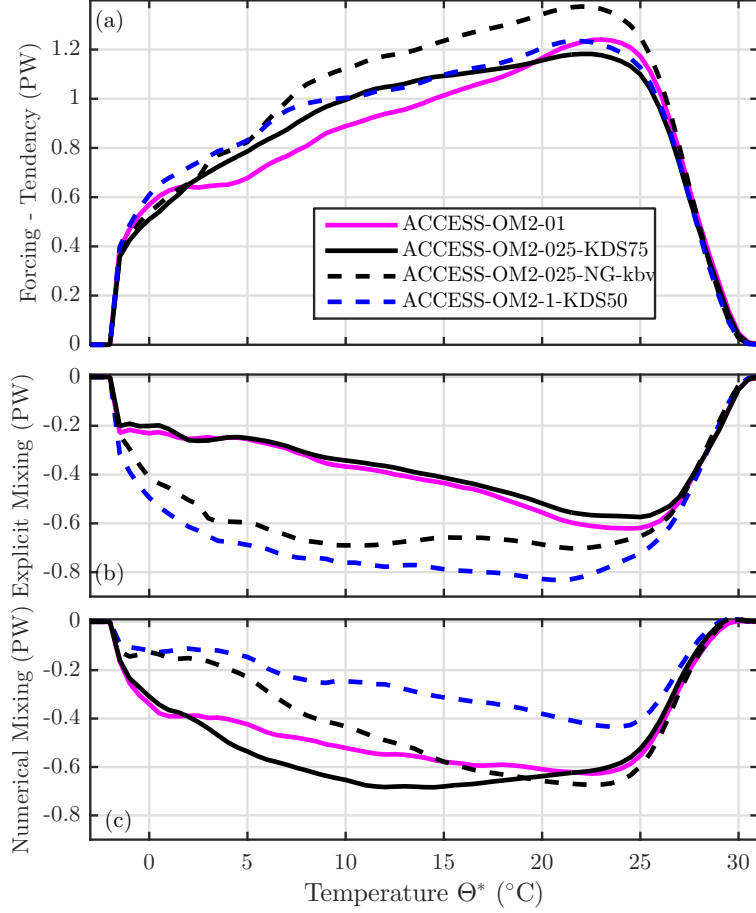


**Figure 14.** Global annually-averaged diathermal heat budget terms (a) surface forcing minus tendency,  $\mathcal{F}^g + \mathcal{P}_I^g - \partial \mathcal{H}_I^g / \partial t$ , (b) explicitly parameterized mixing (neutral and vertical,  $\mathcal{N}^g + \mathcal{M}^g$ ) and (c) numerical mixing,  $\mathcal{I}^g$ , in four configurations chosen to compare across horizontal resolution. ACCESS-OM2-01 and ACCESS-OM2-025-KDS75 share the same vertical grid and explicit mixing parameters, while ACCESS-OM2-025-NG-kbv and ACCESS-OM2-1-KDS50 differ only in that the neutral diffusivity is larger in ACCESS-OM2-1-KDS50. The vertical scale of every panel is the same to facilitate comparison.

difference in neutral diffusion coefficients, the fact that the differences in numerical mixing are larger than the differences in explicit mixing at temperatures warmer than  $\sim 7^\circ\text{C}$  suggests that much of the increase in numerical mixing arises because of the enhanced velocity variability at  $1/4^\circ$  due to its admission of eddy variability.

ACCESS-OM2-025-KDS75 and ACCESS-OM2-01 both share the same vertical grid and the same explicit mixing parameter choices - differing only in their horizontal grid spacing and horizontal viscosity (they both use the same grid-scale dependent Smagorinsky coefficient of  $C = 2$ ). Both configurations show similar levels of explicit mixing, while ACCESS-OM2-025-KDS75 shows slightly enhanced numerical mixing at temperatures characterizing the eddy-rich WBCs and ACC between  $3^\circ\text{C}$  and  $20^\circ$  (compare magenta and black solid lines in Fig. 14c). These differences account for the slightly larger total numerical mixing in ACCESS-OM2-025-KDS75,  $\mathcal{I}_{\text{net}} = 16.3\text{PW}^\circ\text{C}$ , compared to ACCESS-OM2-01,  $\mathcal{I}_{\text{net}} = 14.7\text{PW}^\circ\text{C}$ .

To quantify differences in velocity and temperature variability across scales and between the various horizontal resolution configurations, we plot horizontal kinetic energy and temperature spectra for a region in the Pacific sector of the Southern Ocean across our suite of simulations (Fig. 15). ACCESS-OM2-1-KDS50 shows a steep drop off in kinetic energy at much larger scales than the other resolutions, reflecting the lack of an active eddy field (also see Kiss et al., 2020). In contrast, both the ACCESS-OM2-025 and ACCESS-OM2-01 configurations show a flatter spectrum at scales between  $\sim 200$  km and  $\sim 50$  km. At larger scales in this range the spectral slope may be consistent with the  $k^{-5/3}$  scaling expected for an inverse energy cascade from geostrophic turbulence theory (e.g. Charney, 1971). At smaller scales the slope drops off more steeply. This steep drop likely reflects the role of biharmonic friction. Comparison of spectra between ACCESS-OM2-01 and ACCESS-OM2-01-hvisc, where the Smagorinsky viscosity scaling factor has been increased from 2 to 3, suggests that the viscosity begins to play a role at a scale of about  $10\Delta x$  (compare magenta solid and dashed lines in Fig. 15a, also see Section 5.5). This scale of  $10\Delta x$  is roughly consistent with where the kinetic energy spectrum begins to steepen. However, in ACCESS-OM2-025 there is also a distinct flattening in the kinetic energy spectrum as the grid-scale is approached. This flattening suggests that velocity variance is accumulating near the grid-scale in ACCESS-OM2-025, potentially reflecting the marginal resolution of the eddy field and resulting in enhanced numerical mixing (these scales may be under-dissipated). It is also noteworthy that the ACCESS-OM2-025-NG configuration where the GM scheme is active has reduced kinetic energy across all scales finer than  $\sim 300$  km due to a less active eddy-field, while ACCESS-OM2-025-N shows some slight reduction in kinetic energy at its smallest scales (compare red solid, dotted and dashed lines in Fig. 15a).

The horizontal temperature variability spectra do not show the steepening evident in the kinetic energy spectra at smaller scales, except in ACCESS-OM2-01 at scales comparable to and below the first baroclinic deformation radius (Fig. 15b). This lack of steepening may reflect the absence of any explicit horizontal diffusion operator (apart from the horizontal component of neutral diffusion when it is active). Instead, at scales approaching the grid-scale the horizontal temperature spectra tend to flatten. This flattening could reflect a transition to the viscous Batchelor regime (with an expected slope of  $k^{-1}$ , Batchelor, 1959), or that temperature variance is accumulating near the grid-scale. This near-grid-scale temperature variance may be caused by variable vertical velocities associated with the grid-scale horizontal velocity variability (e.g. Ilicak et al., 2012), resulting in numerical mixing. It is notable that the GM and neutral diffusion schemes have only a small impact on the horizontal temperature variability at scales near the grid-scale (although the presence of GM does reduce temperature variability at larger scales by reducing resolved eddy-stirring, compare red lines in Fig. 15b).

Our comparison between ACCESS-OM2-025-KDS75 and ACCESS-OM2-01 suggests that numerical mixing is enhanced at  $1/4^\circ$  resolution, but only slightly. The marginal resolution of mesoscale eddies at  $1/4^\circ$  may lead to their velocity signatures at the grid-scale being noisy (as suggested by the flattening in their kinetic energy spectra in Fig. 15a). While eddy formation is better resolved at  $1/10^\circ$ , and there appears to be less flattening in the kinetic energy spectrum as the grid-scale is approached, the cascade of temperature variance from large to small scales in eddying regimes always necessitates the dissipation of temperature variance near the grid scale (Roberts & Marshall, 1998). Thus the dependence of numerical mixing on horizontal resolution is not particularly strong.

## 5.5 Lateral Viscosity

As discussed above, numerical mixing is closely linked to near grid-scale variability in the velocity field and therefore is expected to be strongly influenced by the lateral viscosity (S. Griffies et al., 2000; Ilicak et al., 2012). In ACCESS-OM2-01, if the lateral biharmonic viscosity coefficient is increased by increasing the Smagorinsky scaling

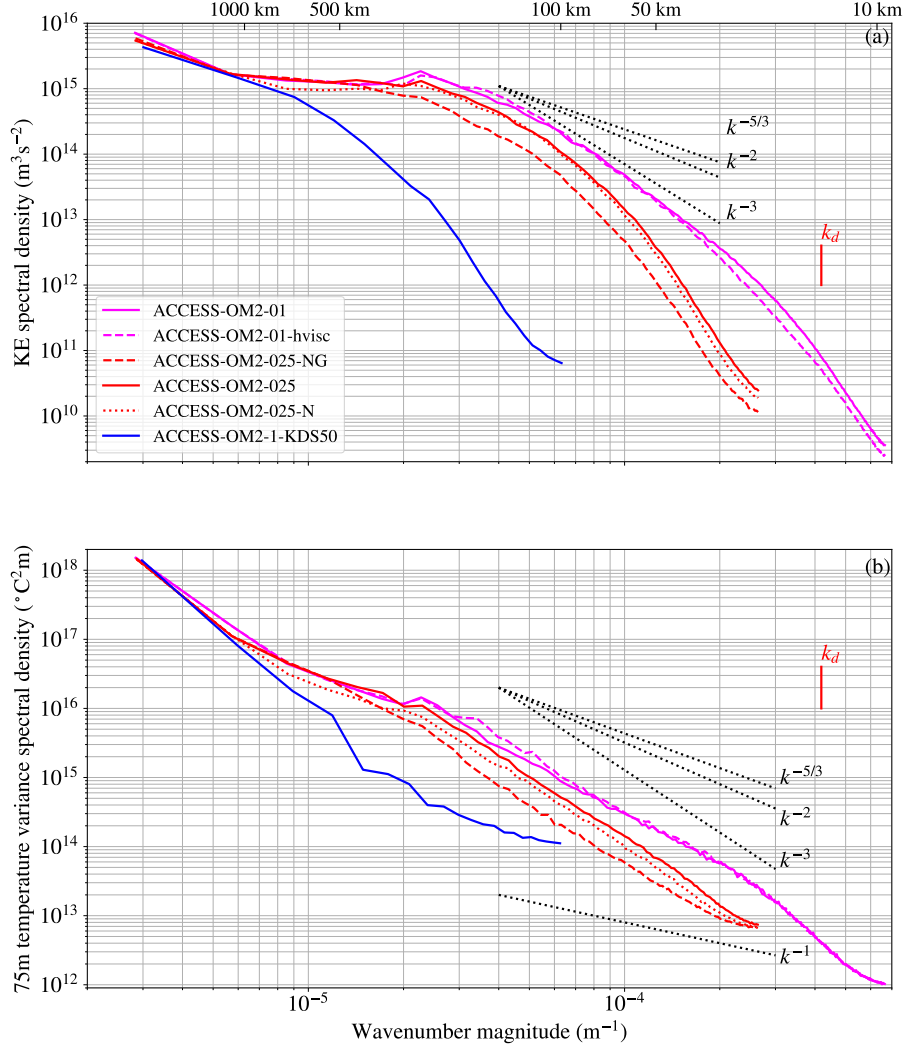


**Figure 15.** Horizontal wavenumber spectra of (a) surface kinetic energy and (b) temperature at 75 m depth from snapshots of the velocity and temperature fields at the end of each month in the Pacific sector of the Southern Ocean (65°S to 45°S, −180°E to −100°E, chosen as it is relatively isotropic and homogeneous) across a range of simulations. The spectra are computed following the methods of Durran et al. (2017) after interpolation onto a uniform Cartesian grid. Reference spectral slopes are shown with the black dotted lines. Corresponding wavelengths are shown at the top. The vertical red line in panel (a) marks the wavenumber  $k_d$  associated with the approximately 15 km first-baroclinic deformation radius in this region (Chelton et al., 1998). Note that the spectra for ACCESS-OM2-025-KDS75 are similar to ACCESS-OM2-025 and spectra for ACCESS-OM2-025-NG-kbv are similar to ACCESS-OM2-025-NG (not shown).



coefficient from 2 to 3 (ACCESS-OM2-01-hvsc in Table 1), there is a 10–15% reduction in numerical mixing across most temperatures (compare magenta solid and dotted lines in Fig. 6i). This reduction is consistent with the results of Ilicak et al. (2012) who found that increasing the Smagorinsky coefficient from 2 to 4 in a  $1/4^\circ$  MOM5 spin-down simulation reduced the spurious numerical mixing by a factor of about 1/3. The reduction in numerical mixing with increased viscosity is associated mainly with regions where eddy variability is high (not shown). Increasing the viscosity in these regions reduces spatial variability in the horizontal velocity at the grid-scale (compare magenta solid and dashed lines in Fig. 15a). However, the changes in viscosity do not influence horizontal temperature variability near the grid-scale (compare magenta solid and dashed lines in Fig. 15b). These changes in numerical mixing are not compensated by changes in vertical mixing (compare magenta lines in Fig. 6e). Instead, the surface temperature structure and surface heat fluxes are altered such that there is less surface heat gain at warmer temperatures and less heat loss at colder temperatures (compare magenta lines in Fig. 6a). However, these changes are not yet in equilibrium due to the short 2 year run-time of ACCESS-OM2-01-hvsc as indicated by enhanced heat loss in the tendency term at colder temperatures (magenta dashed line in Fig. 6c).

## 6 Discussion and Summary

We have presented a method for quantifying the 3D spatial and temporal structure of spurious numerical mixing within global ocean model simulations (Section 2). The method can be applied to any conservative tracer but is here applied to temperature. The method is based on constructing the budget for the “internal heat content” (Holmes, Zika, & England, 2019a) of temperature layers within a given fluid column. The use of internal heat content removes much of the rapid variability in the heat content of temperature layers due to adiabatic and diabatic volume exchanges and therefore reduces the sensitivity of our results to noise compared with previous approaches based on diathermal or diapycnal volume transports (e.g. Lee et al., 2002; Megann, 2017; Urakawa & Hasumi, 2014). Combined with the use of precise online diagnostics, our method provides a detailed view of the spatial structure of numerical mixing within realistically-forced global ocean model simulations (e.g. Fig. 3).

Applied to a suite of global MOM5-based ocean model simulations the method reveals that the contribution of numerical mixing to the global diathermal heat transport from warm to cold water is comparable to, and often larger than, that of the explicitly parameterized vertical and neutral diffusion (Figs. 2,6). These results are consistent with those of Megann (2017) who suggested that numerical mixing in NEMO was comparable or larger than explicit vertical mixing. Heat fluxes due to numerical mixing are largest in the eddying WBCs and ACC, the continental shelves and slopes and the tropical Pacific and Atlantic thermoclines (Fig. 3) where grid-scale horizontal velocity variability and both horizontal and vertical grid-scale temperature variability is largest.

The sensitivity of numerical mixing to various model parameters is summarized in Fig. 16 by comparing the net heat variance dissipation rate diagnostic  $\mathcal{I}_{\text{net}}$  (corresponding to the area under the curve of the global diathermal heat transport due to numerical mixing, see Section 2.6), and its explicit mixing counterpart, across the various configurations. Fig. 16 illustrates the interplay between explicit and numerical mixing, with larger explicit mixing generally leading to smaller numerical mixing and vice versa. In particular, several of the  $1/4^\circ$  configurations and both  $1/10^\circ$  configurations have more numerical mixing than explicit mixing (they lie above the dashed one-to-one line in Fig. 16).

Numerical mixing at colder temperatures in the eddying WBCs and ACC is sensitive to the presence of explicit parameterizations for neutral diffusion and eddy-induced advection (GM) suggesting that a significant proportion is along-isopycnal (Section 5.1,



compare squares, diamonds and circles in Fig. 16). In contrast, numerical mixing in the tropics is more sensitive to the background vertical diffusion and vertical resolution (Sections 5.2 and 5.3, compare symbol size and fill in Fig. 16). Combined with the fact that temperature variations dominate density variations in the tropics, the dependence of numerical mixing on the vertical diffusivity and resolution suggests that much of the numerical mixing in the tropics is diapycnal.

Numerical mixing is also sensitive to horizontal resolution, being smallest at  $1^\circ$  (where mesoscale eddies are largely absent) and largest at  $1/4^\circ$  (compare blue, red and purple symbols in Fig. 16). However, for standard configurations much of these differences are linked to differences in parameterized explicit mixing coefficients. Comparing  $1/4^\circ$  and  $1/10^\circ$  configurations which share the same explicit mixing parameters and vertical resolution suggests that numerical mixing is only slightly enhanced at the  $1/4^\circ$  eddy-permitting resolution (Fig. 14, red and purple circles joined by an arrow in Fig. 16). Our results therefore suggest that while eddies are better resolved at  $1/10^\circ$ , the necessity of dissipating temperature variance at small scales due to its down-scale cascade in eddying regimes (Roberts & Marshall, 1998) means that numerical mixing is not strongly dependent on horizontal resolution once eddies are permitted.

While our current method is unable to quantitatively distinguish between the isopycnal and diapycnal components of numerical mixing it may be possible to generalize our approach by combining the heat and salt budget diagnostics (Hieronimus, Nilsson, & Nycander, 2014; Zika et al., 2015). However, non-linearities in the equation of state may be more difficult to deal with and it is not clear that the properties of the internal heat content budget that we have taken advantage of here could be retained. Our results nevertheless indirectly suggest that the diapycnal component of numerical mixing is not negligible. While in this study we have taken the standard MOM5 numerical tracer advection scheme (MDPPM) as given, our results, along with previous studies (e.g. Ilicak et al., 2012; Megann, 2017) suggest that more attention should be paid to the choice of both numerical tracer advection schemes and horizontal momentum advection and friction parameters in global ocean models.

It is encouraging that increasing the vertical resolution in the tropical ocean reduces numerical mixing there. Increases in the number of vertical levels, or simply changing the placement of the levels, provides an economical way to reduce numerical mixing. However, it is important to note that as numerical mixing is reduced explicit mixing parameters may need to be increased to compensate. The equatorial subsurface temperature biases shown in Fig. 11 suggest that a minimum level of mixing in the upper ocean is required to reproduce the observed hydrographic structure.

While open questions remain, the method and diagnostics presented here provide a clearer geographic view of the impact of numerical discretization on the heat budget of global ocean models, with implications for model biases, heat transport (e.g. Holmes, Zika, Ferrari, et al., 2019) heat uptake (Adcroft et al., 2019) and drift.

## A Appendix A: Numerical details

This appendix describes some numerical details as to how the internal heat content budget is constructed (Section A.1) and discusses some known issues with the method (Section A.2) and their implications (Section A.3).

### A.1 Numerical construction of temperature-coordinate budgets

The terms in the internal heat content budget [Eq. (6)] not involving the lateral fluxes  $\mathcal{Q}$  and  $\Psi$  are calculated as described in HZE19 over a regular temperature grid with  $0.5^\circ\text{C}$  intervals, except here we do not perform a global integral. The lateral terms,

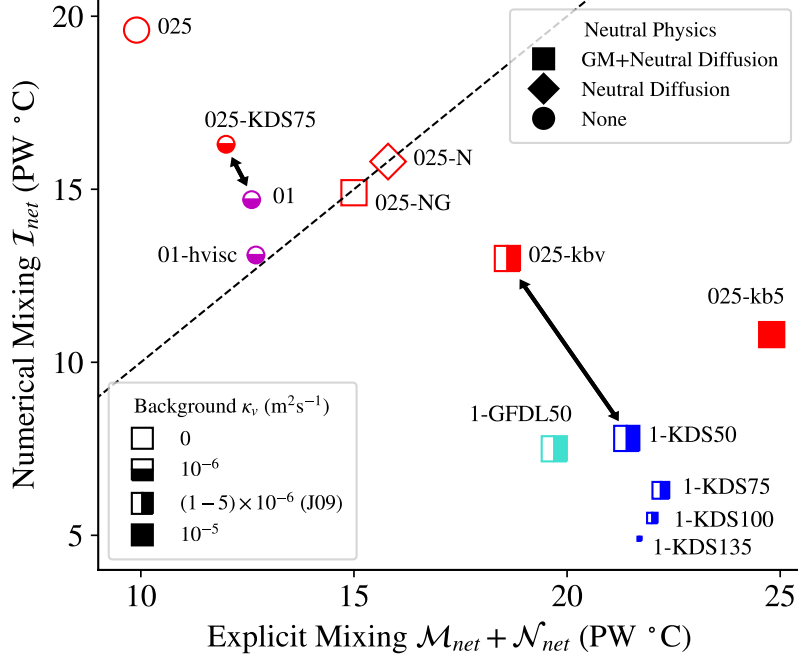


**Figure 16.** A summary of the total amount of numerical (y-axis) and explicitly-parameterized (x-axis) mixing in the various configurations considered in this article as quantified by the net heat variance dissipation rate diagnostic  $\mathcal{I}_{net}$  (see Section 2.6) and its vertical mixing ( $\mathcal{M}_{net}$ ) and neutral mixing ( $\mathcal{N}_{net}$ ) counterparts. Blue, red and purple symbols indicate  $1^\circ$ ,  $1/4^\circ$  and  $1/10^\circ$  configurations respectively. The symbol size is inversely proportional to the number of vertical levels. The different symbol types and symbol fills indicate the active neutral physics parameterizations and background vertical diffusivity, respectively, as indicated in the legends. Models lying above the dashed one-to-one line have more numerical mixing than explicit mixing and vice versa. The two black arrows pair configurations with different horizontal resolutions which have as much as possible equivalent explicit mixing parameters (see Section 5.4 and Fig. 14)

$\mathcal{Q}$  and  $\Psi$ , which vanish when integrated globally, are obtained similarly by binning the Eulerian lateral heat and volume transports at the tracer-cell faces into temperature classes online at every time step, and then summing over all temperatures warmer than  $\Theta^*$ . Note that the binning temperature used for  $\mathcal{Q}$  and  $\Psi$  is the temperature interpolated to the tracer-cell faces where the given flux is located. All terms in Eq. (6) are located on temperature bin edges and no averaging in temperature coordinates is required.

In addition to advective transports associated with the resolved velocity,  $\mathcal{Q}$  and  $\Psi$  should also include terms associated with the eddy parameterizations of Gent and McWilliams (1990, hereafter GM) and Fox-Kemper, Ferrari, and Hallberg (2008). In the simulations considered in this article these parameterizations are formulated in the tracer equations using a skew-diffusive approach (S. M. Griffies, 1998). As described in Appendix B, when using the skew-diffusive lateral heat flux the eddy contribution to  $\mathcal{Q}$  includes a term associated with the eddy-driven lateral volume flux that cancels with the corresponding term in the volume budget when formulating the internal heat content budget. Therefore, our analysis does not use the eddy-driven contribution to  $\Psi$ . While skew-diffusion itself should not drive any heat across isotherms, its numerical implementation may drive across-isotherm heat fluxes which are also captured in  $\mathcal{I}$ . However, we note that a global integral of the full three-dimensional convergence of the skew-diffusive heat fluxes in temperature coordinates suggests that the numerical mixing is dominated by that associated with the resolved velocity field.

## A.2 Known issues

There are several known potential inaccuracies with the spatially-resolved method.

### *Temperature binning of flux convergences*

The temperature binning process assigns all of the heat flux convergence due to a given process to the cell mean temperature, which follows from a finite volume interpretation of the discrete tracer equation. In contrast, the numerical formulation of a given process may implicitly assume that there is some sub-grid-scale structure to the temperature field. Getzlaff et al. (2010) discuss some alternative binning methods.

### *Temperature binning of lateral transports*

The binning of the lateral transports  $\mathcal{Q}$  and  $\Psi$  is performed using the temperature linearly interpolated to the tracer-cell faces while the other terms use the tracer-cell center temperatures. This issue is related to the fundamental constraint on finite-volume advection schemes that the fluxes on cell faces must be related through some interpolation scheme to the non-co-located cell center tracer values. It is possible that improved results could be obtained using a more technically difficult up-winding system where the flux is binned according to the temperature of the tracer cell into which the flux is entering.

### *Temperature binning and time stepping*

The binning of each Eulerian process tendency occurs once per time-step using the value of the temperature field before the time step. This choice is sensible but arbitrary. One could instead use the temperature field after it has been updated. Tests with a toy one-dimensional example (not shown) suggest that this error has a large impact on the binning of the native model total tendency and advection diagnostics (which are not used in the present method), but it does not strongly influence the binning of the other diabatic terms which vary more smoothly in time and space. One exception is the 1-degree model where the base configuration time step is a relatively large fraction of the diurnal cycle and thus the binning does not fully resolve the fast changes in near surface ther-

mal stratification, short-wave penetration and convective mixing (see Section 5.3). It is also worth noting the different approach of Gibson et al. (2017) who perform a reference potential energy calculation between several sub-time step processes in MOM6, allowing the impacts of these different processes to be evaluated separately (in contrast, MOM5 does not use operator splitting - the tracer concentrations are updated only once per time step).

### *The Sea Surface Height (SSH) smoother*

The lateral volume transport achieved by the Laplacian SSH smoothing operator (included to suppress a checkerboard null mode present in B-grid barotropic equations) is not included in the lateral volume flux convergence  $\Psi$  (although the impact of the SSH smoother is included in the heat flux convergence). The missing term leads to residuals in the vertically-integrated volume budget of up to  $\pm 10^{-7} \text{ m s}^{-1}$  in regions where SSH gradients are strong such as the Gulf Stream and ACC (not shown).

### **A.3 Comments on noise, uncertainties and up-gradient fluxes**

Physically based mixing, such as that from a Laplacian diffusion operator, smooths small scale structure. Consequently, a map of the diffusion time tendency exhibits enhanced power at the grid scale; i.e., it is “noisy”. By extension, it is thus not surprising that any diagnosis of spurious mixing from truncation errors can also be prone to noise. The presence of noise makes it difficult to determine a confidence range on our results. The vertically-integrated heat budget closes to much better than  $\pm 1 \text{ W m}^{-2}$ . Similarly, the neglect of the volume transport from the SSH smoother can be estimated using the vertically-integrated volume budget residuals and approximate isotherm depths to have an impact of less than  $\pm 1 \text{ W m}^{-2}$  on  $\mathcal{I}$ . These errors are substantially lower than the  $10 - 100 \text{ W m}^{-2}$  values that we find for the diathermal heat transport due to numerical mixing across intermediate isotherms (Fig. 3). However, it is not trivial to evaluate the impact of the other inaccuracies listed above.

Taking ACCESS-OM2-025 as an example, noise is apparent in  $\mathcal{I}$  at small spatial scales near strong jets and frontal regions, where patches of small-scale large-magnitude positive and negative fluxes can appear (e.g. along the coastal extent of the Gulf Stream, Fig. A.1a). There are also some smaller magnitude up-gradient fluxes along the Equator (e.g. in the Western Pacific, Fig. 3a) which are associated with the coarse vertical grid spacing of the KDS50 grid in those regions (as discussed in Section 5.3). The Suresh and Huynh (1997) flux limiters on the MDPPM scheme should maintain monotonicity in the advected tracer distribution and prevent up-gradient fluxes. These up-gradient fluxes are not associated with the skew-diffusive submesoscale parameterization (established by turning this parameterization off, not shown) or GM or neutral diffusion (which are not active in ACCESS-OM2-025). Therefore, the presence of these small patches of up-gradient fluxes indicates that our method cannot accurately quantify numerical mixing at the grid-scale in these regions due to the approximations discussed above. However, when spatially averaged over larger regions including hundreds of grid points the fluxes are dominantly down-gradient (e.g. Fig. A.1b where the  $1/4^\circ$  map in Fig. A.1a has been conservatively remapped to a coarse  $2.5^\circ$  grid). Further temporal averaging also reduces this noise (not shown). We therefore restrict our analyses to discussing these larger scale patterns (although the spatially-resolved metrics are presented at full resolution).

## **B Appendix B: The role of skew-diffusion in the internal heat content budget**

The Gent and McWilliams (1990) and Fox-Kemper et al. (2008) parameterizations for eddy-driven transport are implemented in the model simulations using a skew-diffusive

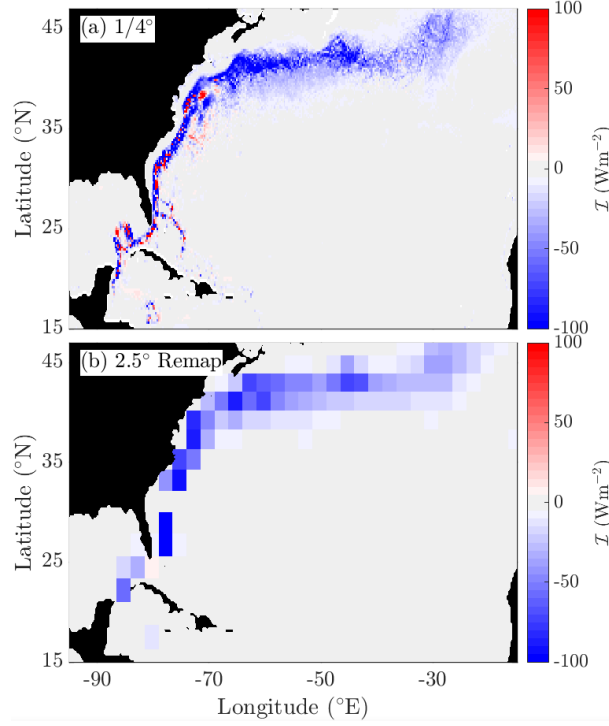


**Figure A.1.** Heat flux through the 15°C isotherm due to numerical mixing in the North Atlantic from ACCESS-OM2-025 at (a) full resolution and (b) conservatively remapped to a coarse 2.5° grid.

formulation as described in S. M. Griffies (1998). In this appendix we discuss the impact of skew-diffusion on the internal heat content budget of temperature layers within fluid columns and contrast it with an advective formulation. We consider a simple example described by Fig. B.1 where a temperature field  $\Theta(y, z, t)$  defined in the meridional-vertical plane consists of isotherms (such as the  $\Theta^*$  isotherm highlighted in orange) that slope upwards toward the north. For simplicity, we will assume that the ocean surface is a rigid lid with no surface volume fluxes, that salinity is constant (such that isopycnals and isotherms are synonymous) and that the only process that influences the temperature field is a parameterized eddy-driven circulation that will act to remove available potential energy by flattening isotherms. The eddy-driven circulation is characterized by a divergence-free eddy-induced velocity  $\mathbf{v}^e$  related to an overturning streamfunction  $\psi^e(y, z, t)$  by,

$$\mathbf{v}^e = -\psi_z^e \hat{\mathbf{j}} + \psi_y^e \hat{\mathbf{k}} \quad (\text{B.1})$$

where  $\hat{\mathbf{j}}$  and  $\hat{\mathbf{k}}$  are unit vectors in the meridional ( $y$ ) and vertical ( $z$ ) directions respectively.

The evolution of the temperature field is described by

$$\rho_0 C_p \frac{\partial \Theta}{\partial t} = -\nabla \cdot \mathbf{Q}, \quad (\text{B.2})$$

where  $\mathbf{Q}$  is the heat flux. An *advective* formulation of the eddy-driven heat flux  $\mathbf{Q}$  is given by

$$\mathbf{Q}^{(A)} = \rho_0 C_p \mathbf{v}^e \Theta = \rho_0 C_p \left( -\psi_z^e \Theta \hat{\mathbf{j}} + \psi_y^e \Theta \hat{\mathbf{k}} \right). \quad (\text{B.3})$$

In the situation described by Fig. B.1 a positive sign for  $\psi^e$  will result in a vector field  $\mathbf{Q}^{(A)}$  (red vectors in Fig. B.1) that flattens isotherms. A *skew-diffusive* formulation for

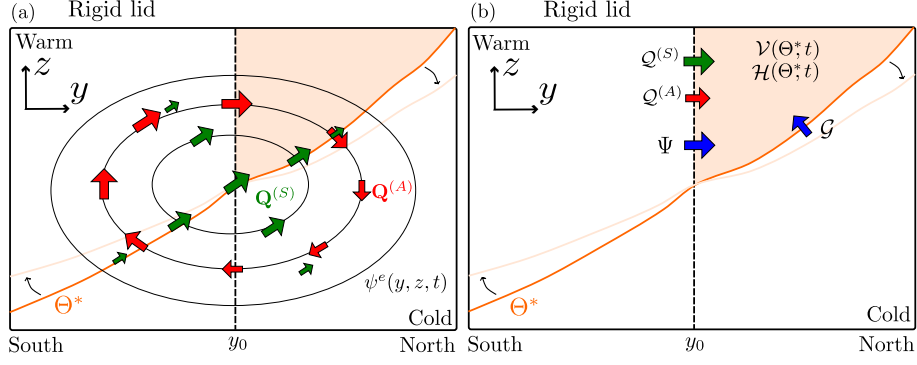


**Figure B.1.** Schematic illustrating the impact of a parametrization for adiabatic eddy-driven tracer transport on the heat and volume budgets of temperature layers. In panel (a) an eddy streamfunction  $\psi^e$  (black contours) acts to flatten isotherms through the convergence of either an advective heat flux  $\mathbf{Q}^{(A)}$  (red vectors) or a skew-diffusive heat flux  $\mathbf{Q}^{(S)}$  (green vectors) whose divergences are equal. Panel (b) denotes various terms in the volume,  $\mathcal{V}(\Theta^*, t)$ , and heat,  $\mathcal{H}(\Theta^*, t)$ , budgets of the region bounded below by the  $\Theta^*$  isotherm, above by the rigid lid and to the south by the fixed latitude  $y_0$ . These terms include the total advective,  $\mathcal{Q}^{(A)}(\Theta^*, t)$ , and skew-diffusive,  $\mathcal{Q}^{(S)}(\Theta^*, t)$ , heat transports across the  $y_0$  latitude at temperatures above  $\Theta^*$ , the volume transport,  $\Psi(\Theta^*, t)$ , across the  $y_0$  latitude at temperatures above  $\Theta^*$  as well as the across-isotherm volume transport  $\mathcal{G}(\Theta^*, t)$  (equal to zero in this adiabatic example).

$\mathbf{Q}$  is instead captured by the heat flux

$$\mathbf{Q}^{(S)} = -\rho_0 C_p \mathbf{K}_S \cdot \nabla \Theta = \rho_0 C_p (\psi^e \Theta_z \hat{\mathbf{j}} - \psi^e \Theta_y \hat{\mathbf{k}}). \quad (\text{B.4})$$

In Eq. (B.4),  $\mathbf{K}_S$  is an anti-symmetric diffusivity tensor with zeros for the diagonal elements and  $\pm\psi^e$  for the off-diagonal elements (e.g. see S. M. Griffies, 1998). The vector field  $\mathbf{Q}^{(S)}$  (green vectors in Fig. B.1) is everywhere parallel to isotherms. It is easy to verify that the heat fluxes  $\mathbf{Q}^{(S)}$  and  $\mathbf{Q}^{(A)}$  differ only by a non-divergent vector field and therefore result in the same evolution of the temperature field.

We now consider the heat and volume budgets of the volume  $\mathcal{V}(\Theta^*, t)$  bounded below by the  $\Theta^*$  isotherm, above by the fixed rigid lid and to the south by the latitude  $y_0$  (orange shaded region in Fig. B.1). The volume of this region evolves according to the motion of its boundaries

$$\frac{\partial \mathcal{V}}{\partial t} = \iint_{\partial \mathcal{V}} \mathbf{v}^b \cdot \hat{\mathbf{n}} dS, \quad (\text{B.5})$$

$$= \iint_{\Theta=\Theta^*} \mathbf{v}^b \cdot \hat{\mathbf{n}} dS, \quad (\text{B.6})$$

where  $\mathbf{v}^b$  is the velocity of points on the boundary  $\partial \mathcal{V}$  of the volume  $\mathcal{V}$  over which the surface integral is performed (Groeskamp et al., 2019; Holmes, Zika, & England, 2019b) and the normal vector  $\hat{\mathbf{n}}$  is always directed out of the volume  $\mathcal{V}$ . In the second line we have used the fact that the rigid lid and the  $y_0$  latitude boundary are fixed in space and thus the only moving boundary is the  $\Theta^*$  isotherm. In this simple adiabatic example the across-isotherm volume transport  $\mathcal{G}(\Theta^*, t)$  must vanish

$$\mathcal{G} = - \iint_{\Theta=\Theta^*} (\mathbf{v}^e - \mathbf{v}^b) \cdot \hat{\mathbf{n}} dS = 0 \quad (\text{B.7})$$

Using this in Eq. (B.6), along with  $\nabla \cdot \mathbf{v}^e = 0$ , yields

$$\frac{\partial \mathcal{V}}{\partial t} = \Psi(\Theta^*, t), \quad (\text{B.8})$$

where  $\Psi(\Theta^*, t)$  is the total volume transport across the  $y_0$  latitude above the  $\Theta^*$  isotherm (Fig. B.1).

The heat content of the region evolves according to

$$\frac{\partial \mathcal{H}}{\partial t} = \frac{\partial}{\partial t} \iiint_V \rho_0 C_p \Theta dV, \quad (\text{B.9})$$

$$= \rho_0 C_p \iiint_V \frac{\partial \Theta}{\partial t} dV + \rho_0 C_p \iint_{\partial V} \Theta \mathbf{v}^b \cdot \hat{\mathbf{n}} dS, \quad (\text{B.10})$$

$$= - \iint_{\partial V} \mathbf{Q} \cdot \hat{\mathbf{n}} dS + \rho_0 C_p \Theta^* \iint_{\Theta=\Theta^*} \mathbf{v}^b \cdot \hat{\mathbf{n}} dS, \quad (\text{B.11})$$

where in the second line we have used the Leibniz integral rule and in the third line we have used the divergence theorem to replace the temperature tendency with the surface integral of the heat flux  $\mathbf{Q}$ . For an advective formulation of the heat flux  $\mathbf{Q}$

$$\frac{\partial \mathcal{H}}{\partial t} = - \iint_{y=y_0} \mathbf{Q}^{(A)} \cdot \hat{\mathbf{n}} dS - \iint_{\Theta=\Theta^*} \mathbf{Q}^{(A)} \cdot \hat{\mathbf{n}} dS + \rho_0 C_p \Theta^* \iint_{\Theta=\Theta^*} \mathbf{v}^b \cdot \hat{\mathbf{n}} dS, \quad (\text{B.12})$$

$$= \mathcal{Q}^{(A)} \quad (\text{advective}) \quad (\text{B.13})$$

where in the second line we have realized that the last two terms cancel (as  $\mathbf{Q}^{(A)} = \rho_0 C_p \mathbf{v}^e \Theta^*$  on the  $\Theta^*$  isotherm) and we have defined the total heat flux across the  $y_0$  latitude as  $\mathcal{Q}^{(A)}$  (Fig. B.1b). Combining Eq. (B.13) with the volume budget (Eq. (B.8)) yields the internal heat content budget  $\mathcal{V}$

$$\frac{\partial \mathcal{H}_I}{\partial t} = \frac{\partial \mathcal{H}}{\partial t} - \rho_0 C_p \Theta^* \frac{\partial \mathcal{V}}{\partial t} = \mathcal{Q}^{(A)} - \rho_0 C_p \Theta^* \Psi \quad (\text{advective}) \quad (\text{B.14})$$

In contrast, for a skew-diffusive formulation of the heat flux  $\mathbf{Q}$  the heat budget is

$$\frac{\partial \mathcal{H}}{\partial t} = - \iint_{y=y_0} \mathbf{Q}^{(S)} \cdot \hat{\mathbf{n}} dS - \iint_{\Theta=\Theta^*} \mathbf{Q}^{(S)} \cdot \hat{\mathbf{n}} dS + \rho_0 C_p \Theta^* \iint_{\Theta=\Theta^*} \mathbf{v}^b \cdot \hat{\mathbf{n}} dS, \quad (\text{B.15})$$

$$= \mathcal{Q}^{(S)} + \rho_0 C_p \Theta^* \Psi \quad (\text{skew-diffusive}) \quad (\text{B.16})$$

where in the second line we have used the fact that  $\mathbf{Q}^{(S)}$  is parallel to isotherms to eliminate the second term, used Eqs. (B.6) and (B.8) for the last term and defined the skew-diffusive heat transport across the  $y_0$  latitude as  $\mathcal{Q}^{(S)}$  (Fig. B.1b). The internal heat content budget is then

$$\frac{\partial \mathcal{H}_I}{\partial t} = \mathcal{Q}^{(S)} \quad (\text{skew-diffusive}) \quad (\text{B.17})$$

Eq. (B.17) shows that the eddy-driven volume flux  $\Psi$  across the  $y_0$  latitude does not appear in the internal heat content budget when using a skew-diffusive formulation in contrast to an advective formulation [Eq. (B.14)]. Of course, the effect on the internal heat content budget of the two formulations is still equivalent, because the skew-diffusive heat flux across the  $y_0$  latitude  $\mathcal{Q}^{(S)}$  (which is the diagnostic that we use to include the effects of skew-diffusion in the internal heat content budget) differs from the advective heat flux across the  $y_0$  latitude  $\mathcal{Q}^{(A)}$  exactly by the factor  $\rho_0 C_p \Theta^* \Psi$ .

## Acknowledgments

We thank Gurvan Madec and Mehmet Ilicak for useful discussions, and Graeme MacGilchrist and Brandon Reichl for valuable comments on the manuscript. We thank K. Stewart for assistance with setting up the ACCESS-OM2-1 configurations. We thank the Consortium for Ocean and Sea-Ice Modelling in Australia (COSIMA) community for their valuable contributions to ACCESS-OM2 development. Modeling and analysis were undertaken using facilities at the National Computational Infrastructure (NCI), which is supported by the Australian Government. The authors are supported by the Australian Research Council (ARC)'s Centre of Excellence for Climate Extremes. J. Zika acknowledges



support from ARC award DP190101173. Upon acceptance, the data required to reproduce the results in this article will be published online at Research Data Australia and the digital object identifier (doi) will be quoted here.

## References

- Adcroft, A., Anderson, W., Balaji, V., Blanton, C., Bushuk, M., Dufour, C. O., ... Zhang, R. (2019). The GFDL global ocean and sea ice model OM4.0: Model description and simulation features. *Journal of Advances in Modeling the Earth System*, 11, 3167–3211. doi: 10.1029/2019MS001726
- Batchelor, G. K. (1959). Small-scale variation of convected quantities like temperature in turbulent fluid Part 1. General discussion and the case of small conductivity. *J. Fluid Mech.*, 5(1), 113–133. doi: 10.1017/S002211205900009X
- Bryan, K., Manabe, S., & Pacanowski, R. C. (1975). A Global Ocean-Atmosphere Climate Model. Part II. The Oceanic Circulation. *J. Phys. Oceanogr.*, 5(1), 30–46. doi: 10.1175/1520-0485(1975)005<0030:AGOACM>2.0.CO;2
- Burchard, H., & Rennau, H. (2008). Comparative quantification of physically and numerically induced mixing in ocean models. *Ocean Model.*, 20(3), 293–311. doi: 10.1016/j.ocemod.2007.10.003
- Charney, J. G. (1971). Geostrophic turbulence. *J. Atmos. Sci.*, 28(6), 1087–1095.
- Chelton, D. B., deSzoeke, R. A., Schlax, M. G., El Naggar, K., & Siwertz, N. (1998). Geographical variability of the first baroclinic Rossby radius of deformation. *J. Phys. Oceanogr.*, 28(3), 433–460. doi: 10.1175/1520-0485(1998)028<0433:GVOTFB>2.0.CO;2
- Colella, P., & Woodward, P. R. (1984). The piecewise parabolic method (ppm) for gas-dynamical simulations. *J. Comput. Phys.*, 54(1), 174–201. doi: 10.1016/0021-9991(84)90143-8
- Durran, D., Weyn, J. A., & Menchaca, M. Q. (2017). Practical considerations for computing dimensional spectra from gridded data. *Mon. Wea. Rev.*, 145(9), 3901–3910. doi: 10.1175/MWR-D-17-0056.1
- Fox-Kemper, B., Adcroft, A., Boning, C. W., Chassignet, E. P., Curchitser, E., Danabasoglu, G., ... Yeager, S. G. (2019). Challenges and prospects in ocean circulation models. *Frontiers in Marine Science*, 6, 65. doi: 10.3389/fmars.2019.00065
- Fox-Kemper, B., Ferrari, R., & Hallberg, R. (2008). Parameterization of mixed layer eddies. Part I: Theory and diagnosis. *J. Phys. Oceanogr.*, 38(6), 1145–1165. doi: 10.1175/2007JPO3792.1
- Gent, P. R., & McWilliams, J. C. (1990). Isopycnal mixing in ocean circulation models. *J. Phys. Oceanogr.*, 20(1), 150–155. doi: 10.1175/1520-0485(1990)020<0150:IMIOCM>2.0.CO;2
- Getzlaff, J., Nurser, G., & Oschlies, A. (2010). Diagnostics of diapycnal diffusivity in z-level ocean models part I: 1-Dimensional case studies. *Ocean Model.*, 35(3), 173–186. doi: 10.1016/j.ocemod.2010.07.004
- Gibson, A. H., Hogg, A. M., Kiss, A. E., Shakespeare, C. J., & Adcroft, A. (2017). Attribution of horizontal and vertical contributions to spurious mixing in an Arbitrary Lagrangian-Eulerian ocean model. *Ocean Model.*, 119, 45–56. doi: 10.1016/j.ocemod.2017.09.008
- Griffies, S., Adcroft, A., Banks, H., Böning, C., Chassignet, E., Danabasoglu, G., ... others (2009). Problems and prospects in large-scale ocean circulation models. *Proceedings of OceanObs*, 9, 410–431.
- Griffies, S., Pacanowski, R., & Hallberg, R. (2000). Spurious diapycnal mixing associated with advection in a z-coordinate ocean model. *Mon. Wea. Rev.*, 128(3), 538–564. doi: 10.1175/1520-0493(2000)128<0538:SDMAWA>2.0.CO;2
- Griffies, S. M. (1998). The Gent-McWilliams skew flux. *J. Phys. Oceanogr.*, 28(5), 831–841. doi: 10.1175/1520-0485(1998)028<0831:TGMSF>2.0.CO;2

- Griffies, S. M. (2004). *Fundamentals of ocean climate models* (Vol. 518). Princeton university press Princeton.
- Griffies, S. M. (2012). Elements of the modular ocean model (MOM). *GFDL Ocean Group Tech. Rep*, 7, 620.
- Griffies, S. M., Gnanadesikan, A., Dixon, K. W., Dunne, J. P., Gerdes, R., Harrison, M. J., ... Zhang, R. (2005). Formulation of an ocean model for global climate simulations. *Ocean Science*, 1(1), 45-79.
- Griffies, S. M., & Hallberg, R. W. (2000). Biharmonic friction with a smagorinsky-like viscosity for use in large-scale eddy-permitting ocean models. *Mon. Wea. Rev.*, 128(8), 2935-2946. doi: 10.1175/1520-0493(2000)128<2935:BFWASL>2.0.CO;2
- Griffies, S. M., Winton, M., Anderson, W. G., Benson, R., Delworth, T. L., Dufour, C. O., ... Zhang, R. (2015). Impacts on ocean heat from transient mesoscale eddies in a hierarchy of climate models. *J. Climate*, 28(3), 952-977. doi: 10.1175/JCLI-D-14-00353.1
- Groeskamp, S., Griffies, S. M., Iudicone, D., Marsh, R., Nurser, A. G., & Zika, J. D. (2019). The water mass transformation framework for ocean physics and biogeochemistry. *Annual Review of Marine Science*, 11(1), 271-305. doi: 10.1146/annurev-marine-010318-095421
- Hallberg, R. (2013). Using a resolution function to regulate parameterizations of oceanic mesoscale eddy effects. *Ocean Model.*, 72, 92 - 103. doi: 10.1016/j.ocemod.2013.08.007
- Hecht, M. W. (2010). Cautionary tales of persistent accumulation of numerical error: Dispersive centered advection. *Ocean Model.*, 35(3), 270 - 276. doi: 10.1016/j.ocemod.2010.07.005
- Hieronimus, M., Nilsson, J., & Nycander, J. (2014). Water mass transformation in salinity-temperature space. *J. Phys. Oceanogr.*, 44(9), 2547-2568. doi: 10.1175/JPO-D-13-0257.1
- Hill, C., Ferreira, D., Campin, J.-M., Marshall, J., Abernathey, R., & Barrier, N. (2012). Controlling spurious diapycnal mixing in eddy-resolving height-coordinate ocean models—insights from virtual deliberate tracer release experiments. *Ocean Model.*, 45, 14-26.
- Holmes, R. M., Zika, J. D., & England, M. H. (2019a). Diathermal heat transport in a global ocean model. *J. Phys. Oceanogr.*, 49(1), 141-161. doi: 10.1175/JPO-D-18-0098.1
- Holmes, R. M., Zika, J. D., & England, M. H. (2019b). Reply to 'Comments on "Diathermal heat transport in a global ocean model"'. *J. Phys. Oceanogr.*, 49(8), 2195-2197. doi: 10.1175/JPO-D-19-0139.1
- Holmes, R. M., Zika, J. D., Ferrari, R., Thompson, A. F., Newsom, E. R., & England, M. H. (2019). Atlantic ocean heat transport enabled by indo-pacific heat uptake and mixing. *Geophys. Res. Lett.*, 46(23), 13939-13949. doi: 10.1029/2019GL085160
- Ilicak, M. (2016). Quantifying spatial distribution of spurious mixing in ocean models. *Ocean Model.*, 108, 30 - 38. doi: 10.1016/j.ocemod.2016.11.002
- Ilicak, M., Adcroft, A. J., Griffies, S. M., & Hallberg, R. W. (2012). Spurious diapycnal mixing and the role of momentum closure. *Ocean Model.*, 45-46, 37-58. doi: 10.1016/j.ocemod.2011.10.003
- Jochum, M. (2009). Impact of latitudinal variations in vertical diffusivity on climate simulations. *J. Geophys. Res.*, 114(C1). doi: 10.1029/2008JC005030
- Kiss, A. E., Hogg, A. M., Hannah, N., Boeira Dias, F., Brassington, G. B., Chamberlain, M. A., ... Zhang, X. (2020). ACCESS-OM2 v1.0: a global ocean-sea ice model at three resolutions. *Geosci. Model Dev.*, 13(2), 401-442. doi: 10.5194/gmd-13-401-2020
- Klingbeil, K., Mohammadi-Aragh, M., Gräwe, U., & Burchard, H. (2014). Quantification of spurious dissipation and mixing—discrete variance decay in a finite-

- 1125 volume framework. *Ocean Model.*, 81, 49–64.
- 1126 Large, W. G., McWilliams, J. C., & Doney, S. C. (1994). Oceanic vertical mixing:  
1127 A review and a model with a nonlocal boundary layer parameterization. *Rev.*  
1128 *Geophys.*, 32(4), 363–403. doi: 10.1029/94RG01872
- 1129 Ledwell, J. R., Laurent, L. C. S., Giron, J. B., & Toole, J. M. (2011). Diapycnal  
1130 mixing in the Antarctic Circumpolar Current. *J. Phys. Oceanogr.*, 41(1), 241–  
1131 246. doi: 10.1175/2010JPO4557.1
- 1132 Lee, M.-M., Coward, A. C., & Nurser, A. J. G. (2002). Spurious diapycnal mixing of  
1133 the deep waters in an eddy-permitting global ocean model. *J. Phys. Oceanogr.*,  
1134 32(5), 1522–1535. doi: 10.1175/1520-0485(2002)032<1522:SDMOTD>2.0.CO;2
- 1135 Leonard, B. (1984). Third-order upwinding as a rational basis for computational  
1136 fluid dynamics. *Computational techniques and applications: CTAC-83*, 106–  
1137 120.
- 1138 Maqueda, M. M., & Holloway, G. (2006). Second-order moment advection scheme  
1139 applied to Arctic Ocean simulation. *Ocean Model.*, 14(3), 197 - 221. doi: 10  
1140 .1016/j.ocemod.2006.05.003
- 1141 Marchesiello, P., Debreu, L., & Couvelard, X. (2009). Spurious diapycnal mix-  
1142 ing in terrain-following coordinate models: The problem and a solution. *Ocean*  
1143 *Model.*, 26(3), 156 - 169. doi: 10.1016/j.ocemod.2008.09.004
- 1144 Marshall, J., Jamous, D., & Nilsson, J. (1999). Reconciling thermodynamic and dy-  
1145 namic methods of computation of water-mass transformation rates. *Deep-Sea*  
1146 *Res. I*, 46(4), 545 - 572. doi: 10.1016/S0967-0637(98)00082-X
- 1147 McDougall, T. J. (2003). Potential enthalpy: A conservative oceanic variable for  
1148 evaluating heat content and heat fluxes. *J. Phys. Oceanogr.*, 33(5), 945–963.  
1149 doi: 10.1175/1520-0485(2003)033<0945:PEACOV>2.0.CO;2
- 1150 McDougall, T. J., & Barker, P. M. (2011). Getting started with TEOS-10 and the  
1151 Gibbs Seawater (GSW) oceanographic toolbox. *SCOR/IAPSO WG*, 127, 1–  
1152 28.
- 1153 McDougall, T. J., Groeskamp, S., & Griffies, S. M. (2014). On geometrical aspects of  
1154 interior ocean mixing. *J. Phys. Oceanogr.*, 44(8), 2164–2175. doi: 10.1175/JPO  
1155 -D-13-0270.1
- 1156 Megann, A. (2017). Estimating the numerical diapycnal mixing in an eddy-  
1157 permitting ocean model. *Ocean Model.*, -. doi: 10.1016/j.ocemod.2017.11.001
- 1158 Naughten, K. A., Galton-Fenzi, B. K., Meissner, K. J., England, M. H., Brassington,  
1159 G. B., Colberg, F., ... Debernard, J. B. (2017). Spurious sea ice formation  
1160 caused by oscillatory ocean tracer advection schemes. *Ocean Model.*, 116, 108 -  
1161 117. doi: 10.1016/j.ocemod.2017.06.010
- 1162 Redi, M. H. (1982). Oceanic isopycnal mixing by coordinate rotation. *J. Phys.*  
1163 *Oceanogr.*, 12(10), 1154–1158. doi: 10.1175/1520-0485(1982)012<1154:  
1164 OIMBCR>2.0.CO;2
- 1165 Richter, I. (2015). Climate model biases in the eastern tropical oceans: causes,  
1166 impacts and ways forward. *Wiley Interdisciplinary Reviews: Climate Change*,  
1167 6(3), 345–358. doi: 10.1002/wcc.338
- 1168 Riemenschneider, U., & Legg, S. (2007). Regional simulations of the Faroe Bank  
1169 Channel overflow in a level model. *Ocean Model.*, 17(2), 93 - 122. doi: 10  
1170 .1016/j.ocemod.2007.01.003
- 1171 Roberts, M., & Marshall, D. (1998). Do We Require Adiabatic Dissipation Schemes  
1172 in Eddy-Resolving Ocean Models? *J. Phys. Oceanogr.*, 28(10), 2050–2063. doi:  
1173 10.1175/1520-0485(1998)028<2050:DWRADS>2.0.CO;2
- 1174 Simmons, H. L., Jayne, S. R., Laurent, L. C. S., & Weaver, A. J. (2004). Tidally  
1175 driven mixing in a numerical model of the ocean general circulation. *Ocean*  
1176 *Model.*, 6(3), 245–263. doi: 10.1016/S1463-5003(03)00011-8
- 1177 Smith, K. S., & Ferrari, R. (2009). The production and dissipation of compensated  
1178 thermohaline variance by mesoscale stirring. *J. Phys. Oceanogr.*, 39(10), 2477–  
1179 2501. doi: 10.1175/2009JPO4103.1

- 1180 Solomon, H. (1971). On the Representation of Isentropic Mixing in Ocean Circula-  
1181 tion Models. *J. Phys. Oceanogr.*, 1(3), 233-234. doi: 10.1175/1520-0485(1971)  
1182 001<0233:OTROIM>2.0.CO;2
- 1183 Soufflet, Y., Marchesiello, P., Lemarié, F., Jouanno, J., Capet, X., Debreu, L., &  
1184 Benschila, R. (2016). On effective resolution in ocean models. *Ocean Model.*,  
1185 98, 36 - 50. doi: 10.1016/j.ocemod.2015.12.004
- 1186 Stewart, K., & Hogg, A. (2019). Southern ocean heat and momentum uptake are  
1187 sensitive to the vertical resolution at the ocean surface. *Ocean Model.*, 143,  
1188 101456. doi: <https://doi.org/10.1016/j.ocemod.2019.101456>
- 1189 Stewart, K., Hogg, A., Griffies, S., Heerdegen, A., Ward, M., Spence, P., & England,  
1190 M. (2017). Vertical resolution of baroclinic modes in global ocean models.  
1191 *Ocean Model.*, 113, 50 - 65. doi: 10.1016/j.ocemod.2017.03.012
- 1192 Stewart, K., Kim, W., Urakawa, S., Hogg, A., Yeager, S., Tsujino, H., ... Danaba-  
1193 soglu, G. (2019). Jra55-do-based repeat year forcing datasets for driving ocean-  
1194 sea-ice models. *Ocean Model.*, 101557. doi: 10.1016/j.ocemod.2019.101557
- 1195 Suresh, A., & Huynh, H. (1997). Accurate monotonicity-preserving schemes with  
1196 Runge-Kutta time stepping. *J. Comput. Phys.*, 136(1), 83 - 99. doi: 10.1006/  
1197 jcph.1997.5745
- 1198 Tsujino, H., Urakawa, S., Nakano, H., Small, R. J., Kim, W. M., Yeager, S. G., ...  
1199 others (2018). JRA-55 based surface dataset for driving ocean-sea-ice models  
1200 (JRA55-do). *Ocean Model.*, 130, 79–139.
- 1201 Urakawa, L. S., & Hasumi, H. (2014). Effect of numerical diffusion on the water  
1202 mass transformation in eddy-resolving models. *Ocean Model.*, 74, 22 - 35. doi:  
1203 10.1016/j.ocemod.2013.11.003
- 1204 Walin, G. (1982). On the relation between sea-surface heat flow and thermal cir-  
1205 culation in the ocean. *Tellus*, 34(2), 187–195. doi: 10.1111/j.2153-3490.1982  
1206 .tb01806.x
- 1207 Warner, S. J., Holmes, R., McHugh Hawkins, E. H., Hoecker-Martinez, M., Sav-  
1208 age, A. C., & Moum, J. N. (2018). Buoyant gravity currents released  
1209 from tropical instability waves. *J. Phys. Oceanogr.*, 48, 361-382. doi:  
1210 10.1175/JPO-D-17-0144.1
- 1211 Zika, J. D., Skliris, N., Nurser, A. G., Josey, S. A., Mudryk, L., Laliberté, F.,  
1212 & Marsh, R. (2015). Maintenance and broadening of the ocean’s salin-  
1213 ity distribution by the water cycle. *J. Climate*, 28(24), 9550–9560. doi:  
1214 10.1175/JCLI-D-15-0273.1